Decadal-scale climate cycles preserved in megaherbivore dental tissues in tropical Asia

Louys, Julien[1*]; Miszkiewicz, Justyna J.[2,3]; Higgins, Penny[4], Mathieu Duval[1,5,6], Zaim, Yahdi[7,8]; Puspaningrum, Mika R.[7]; Rizal, Yan[7]; Aswan[7]; Rowe, Joshua[1]; Basilia, Pauline[1]; Loïc Martin[9]; Breitenbach, Sebastian F.M.[10]; Price, Gilbert J.[11]

[1]Australian Research Centre for Human Evolution, Griffith University, Brisbane, Australia

[2]School of Social Science, The University of Queensland, Brisbane, Australia

[3]Earth, Life, Time Group, Naturalis Biodiversity Center, Leiden, The Netherlands

[4] EPOCH Isotopes, 6606 E Townline Rd, Williamson, NY 14589, USA

[5]Centro Nacional de Investigación sobre la Evolución Humana (CENIEH), Paseo Sierra de Atapuerca 3, 09002 Burgos, España

[6]Palaeoscience Labs, Department of Archaeology and History, La Trobe University, Melbourne, Australia

[7]Paleontology and Quaternary Geology Research Group, Faculty of Earth Sciences and Technology, Institut Teknologi Bandung, Bandung, Indonesia

[8]Department of Geology, Institute of Technology Sumatera (ITERA), Lampung, Indonesia

[9]Institute for Geology, University of Innsbruck, Innsbruck, Austria

[10]School of Geography and Natural Sciences, Northumbria University, Newcastle Upon Tyne, UK

[11]School of the Environment, The University of Queensland, Brisbane, Australia

*Corresponding author: j.louys@griffith.edu.au

Keywords: *Elephas maximus,* Bangka Island, Southeast Asia, sunspots, monsoon

Abstract

Rainforests have emerged as key biomes for understanding the initial dispersal of modern humans from Africa[1]. In Southeast Asia, the oldest dated records of humans are associated with rainforests[2-3], but recent fossil records suggest these biomes were structurally different from today[4-5]. Climatic fluctuations associated with insolation changes brought about smooth transitions between rain, dry and montane forests due to impacts of glacial-interglacial and solar cycles on the Asian-Australian monsoon[5-7]. However, the timing and nature of these changes remain poorly understood due to a lack of fossil archives resolved to seasonal or annual scales from the largely submerged Sunda Shelf. Here, we show that large megaherbivore dental tissues record Schwabe sunspot cycles. We demonstrate that $\delta^{13}C$ and $\delta^{18}O$ in a modern African elephant tusk are significantly correlated with insolation changes over solar cycles 21 and 23. Based on this relationship, we examine sunspot cycles in fossil elephant teeth from Bangka Island, one of the emergent Sunda islands at southern end of the so-called savannah corridor. Combined U-series and ESR dating indicates the teeth are early Holocene, and bulk $\delta^{13}C$ and $\delta^{18}O$ values show the elephant lived in wet rainforests. Periodicity analyses suggest that sunspot activity peaked at the beginning and end of tooth enamel formation, associated with higher $\delta^{13}C$ and lower $\delta^{18}O$. The presented specimens indicate that a modern rainforest and monsoonal system, whereby a negative Indian Ocean Dipole coupled with La Niña produces higher regional precipitation, was in place by the early Holocene in Island Southeast Asia.

Introduction

The rainforests of Southeast Asia have emerged as key biomes for understanding the initial dispersal of modern humans and the long-term impact of climatic and environmental change on tropical ecosystems. The traditional idea that ancient tropical forests in Asia were ‘pristine’, ‘natural’, and ‘wild’ has been increasingly challenged by key fossil sites that demonstrate modern humans occupied rainforests much earlier than initially thought[2-3]. The common image of ‘jungles’—at once homogeneous and continuous—masks the enormous heterogeneity present both within and between major tropical forests and the diverse range of Quaternary environments[4-5]. Yet, despite the increasingly recognised importance attributed to these ecosystems[1], there is still very limited understanding of these biomes: how they were structured, how they responded to past climatic changes, and how they may have differed from the environments found in tropical Asia today. Fluctuations in temperature, precipitation (amount, seasonal distribution), cloudiness, geology, and CO_2 concentration have all impacted tropical forests through time and in ways we still do not fully comprehend. This is due in large part to a dearth of fossil records, proxy reconstructions, and geochemical analyses targeting these ecosystems. How tropical forests changed through time is thus a critical gap in our knowledge, especially as current exploitation and destruction of rainforests is one of the most pressing environmental concerns we face[8].

A key source of information for reconstructing ancient environments in Southeast Asia has been fossil mammals preserved in caves (e.g., refs.[9-11]). These fossils, although largely consisting of isolated teeth and tooth crowns of medium- to large-bodied mammals, have provided important insights into broad patterns of regional environmental change and allowed correlations with pan-regional climatic changes such as the impacts of glacial-interglacial temperature and precipitation adjustments on biome shifts[4,9-11]. Other independent proxies for palaeo-environmental and -climate reconstructions in the region remain relatively rare: pollen records dating to the late Quaternary provide important, and often very fine-grained, environmental information[4], but are rarely resolved to seasonal or annual scales and often sourced from sites at considerable distance from areas of interest such as vertebrate fossil deposits. The same problem can be found in speleothem records (e.g., refs.[12-13]), with very few stalagmites from Island Southeast Asia reported in any detail[12-19].

Thus, faunal remains often provide the most proximal and plentiful source of palaeoenvironmental information in Southeast Asia. Megaherbivores especially are, due to their large size, an important but underused resource, as they can preserve daily to annual timeseries of environmental changes at a scale not preserved in smaller species or through stratigraphic sections. Here, we present directly dated, serially sampled enamel stable carbon and oxygen isotope values from specimens of the Asian Elephant, *Elephas maximus,* from the island of Bangka, situated southeast of Sumatra. Bangka is a rare, fossil-bearing emergent island situated in the Sunda Shelf and at the southern end of the so-called 'savannah corridor'[5] (Fig. 1). It is thus at a key locale for understanding regional-scale climate shifts in the late Quaternary but is devoid of any karst outcrops that would preserve speleothems[20]. We compare our isotope results with those of other proboscideans and use these to link cyclical environmental signals with recurrent climatic processes known to impact monsoonal systems to reconstruct palaeoclimate and palaeoenvironments on the Sunda Shelf.

Results

U-series and ESR dating

Full solution U-series, ESR data, and dose rate considerations are provided in the Supplementary Information. Initial combined U-series/ESR age calculation using DATA did not return any finite result. Assuming an early uptake (EU), linear uptake (LU) or closed-system U-series uptake (CSUS) yielded very similar ages ranging from 5 ± 2 ka to 7.9 ± 0.7 ka. Importantly, the gamma dose rate accounted for ~97% of the EU-LU total dose rate. In other words, dental tissues carry negligible weight (<1 %) in the total dose rate evaluation given their very low uranium concentrations and the large initial and removed thicknesses for the enamel layer, which strongly reduced the beta dose rate. The uncertainty on the uranium uptake modelling is minimal and was therefore ignored.

Consequently, the accuracy of the ESR age calculation relied almost entirely on properly constraining the gamma dose rate. Initial calculations based on a gamma dose rate derived from average

radioelement concentrations yielded an ESR age of 7.83 ± 1.19 ka (Table S5 and Extended Table 1). When using a gamma dose rate derived from a single sediment sample instead, ESR age estimates ranged from 3.68 ± 0.56 to 22.0 ± 3.24 ka (Extended Table 1), constraining the fossils to the latest part of the Late Pleistocene and the Holocene. In comparison, the variation of the long-term sediment depth between 1 m and 40 m had a minimal impact on the calculated ESR age (< 1 ka; Extended Table 1). The ESR results being younger than the apparent U-series ages may indicate that dental tissues have all experienced uranium leaching. In other words, the apparent U-series ages may not be regarded as providing reliable minimum age constraints. Thus, there is currently no evidence supporting an age older than the latest Late Pleistocene to Holocene for these fossils, since it would require an extremely low gamma dose rate value (i.e. 10 times lower than that derived from sediment sample BAN19-1, to reach an ESR age compatible with the Middle Pleistocene). Our sensitivity tests indicate that the age of the assemblage is most likely somewhere between 3.7 and 22 ka, with an early Holocene age of around 7.8 ka probably the most reasonable estimate.

Histology

On average, the observed enamel cross-striation width was 2.9 µm. The angle between EDJ and the nearest Retzius line was 6.320 degrees and 45.996 degree to the enamel rods. The average calculation of enamel extension rate was 16.5 µm, which is ca. 6.019 mm per year. Extended Table 2 summarises descriptive statistics for these averages. Extended Table 3 shows a comparison of enamel histology variables collected in our study for *E. maximus* with *M. columbi* and *P. cypriotes* as extracted from published sources[21-25], in addition to estimated body masses and ages where known (unknown for *E. maximus*). The mean enamel extension rate estimate in mm per year for *E. maximus* falls between *P. cypriotes* and *M. columbi,* fitting the pattern expected from estimated body masses, with *P. cypriotes* being the smallest and *M. columbi* the largest.

Carbon and oxygen isotope ratios

Of the 76 samples drilled, only 67 produced reliable results (Table S11). Carbon isotope values ranged from -14.3‰ in BAN19-8 to -16.4‰ in BAN19-9. These values place it well within the closed forest isospace of Southeast Asian mammals (Extended Figure 1 and ref.[3]). Oxygen isotope values ranged from -7.0‰ in BAN19-8 and BAN19-9 to -9.4‰ in in BAN19-8, well within the wettest parts of the Southeast Asian isospace (Extended Figure 1 and ref.[3]).

Periodicity analyses

An examination of periodicity in the carbon and oxygen isotopes using spectral analysis revealed no frequencies that approached 0.05 significance levels (Extended Table 4). These results were compared with the only other known serially sampled Asian elephant post-canines, a DP4 (IVPP V 22700.01) and two M1s (V 22700.02 and V 22700.03) from the Late Pleistocene site of Baxian Cave, South

China[26]. These teeth do preserve significant periodicity at $\alpha = 0.05$: V 22700.02 for both $\delta^{13}C$ and $\delta^{18}O$ (at 92.8 mm and 74.2 mm, respectively), and $\delta^{18}O$ only in V 22700.03 (at 41.0 mm). The periodicity observed in V 22700.02 approaches the frequencies with the highest power for two of our Bangka specimens, BAN19-9 and BAN19-10 (Extended Table 5).

To further explore whether there was any cyclicity in our samples, we attempted to fit a sinusoidal model to each of our serially sampled teeth, using the periodicities observed in the Baxian Cave samples and those from the spectral analysis for each corresponding tooth (Extended Table 4). Reinforcing our observations above, sinusoidal models fit our data for BAN19-9 and BAN19-10 significantly for periods corresponding to between 92.8 mm to 107.7 mm for $\delta^{13}C$, with AIC values unable to discriminate the highest performing model. For $\delta^{18}O$, only BAN19-10 produced significant sinusoidal models, in this case both p-value and AIC were notably smaller for 74.2 mm cyclicity than 67.2 mm. These significant cyclicities of 92.8 mm, 107.7 mm, 74.2 mm, and 67.2 mm, correspond to periods of 15.4, 17.9, 12.3, and 11.2 years using the growth rate of Asian elephant enamel calculated above. These periods approach or correspond to the periodicity in Schwabe sunspot cycles, which have an average periodicity of 11 years but with a standard deviation of approximately 14 months[27].

The best statistical support for a common cause of these cycles was calculated from the Baxian Cave specimen V 22700.02, with peaks in carbon and oxygen isotope values 15 and 12 years apart, respectively. To independently examine whether Schwabe sunspot cycles could be preserved in elephant dental tissues, we compared previously published quasi-weekly sampled carbon and oxygen isotope values from a modern African elephant tusk, calibrated to month, day and year[28], with the average number of sunspots for the tuned days between sampling intervals (sunspot data from ref.[29]), up to a maximum of 7 days prior to the sampled tuned date. There is a significant positive relationship between $\delta^{13}C$ and average sunspot number at the 0.1 level for R37-412 ($p = 0.08$), a portion of the tusk which grew during solar cycle 21, while $\delta^{18}O$ has a significantly positive relationship at the 0.05 significance level ($p = 0.03$). For the combined R37-1169 and R37-1053 tusk, which formed during sun cycle 23, there is a significant positive relationship between both stable isotopes and sunspot number at the 0.001 level ($\delta^{13}C$ $p < 0.001$; $\delta^{18}O$ $p < 0.001$). Finally, examining whether the average periodicity of solar cycles (11 years, equivalent to 66.2 mm along the tooth row) is significantly correlated with our Bangka isotopes using sinusoidal fit indicates that it significantly explains 32% of the $\delta^{13}C$ of BAN19-8 and 49% of BAN19-10, and 46% of the $\delta^{18}O$ of BANG19-10 at the 0.05 significance level.

Discussion

Stable oxygen and carbon isotopes from the Bangka Island elephant teeth indicate that a wet and closed canopy forest was present on the island since at least the onset of the Holocene. Bangka Island is of significance as it sits well within the Southeast Asian Pleistocene savannah corridor, a zone of

seasonally dry tropical forests and open flora that facilitated the persistence and migration of a variety of fauna including early humans[3-5]. The inferred palaeoenvironmental scenario of a wet early Holocene climate and closed tropical forest in this island is consistent with offshore pollen data from the Banda Sea that suggests wetter conditions after 11 ka[30]. It also agrees with speleothem-based stable isotope records from Liang Bua, Flores, indicating an early Holocene monsoon intensification from 11 to 7 ka[18,31], and speleothem records from northwestern Australia and southern China showing a strong early Holocene Asian-Australian Summer monsoon[6,32-33].

Terrestrial archives recording monsoonal dynamics for this part of the world are rare[31], and our observation that the stable isotope records of fossil elephant teeth may preserve solar-forced climatic changes is a new and important contribution to palaeoclimatology. The link between solar cycles, and monsoon activity is well established[6-7,34] and has been observed in numerous speleothem $\delta^{18}O$ records[6,12,35-36] including those of the 11-year sunspot cycle[37]. Models suggest that solar activity in the northeastern Pacific induces sea surface temperature anomalies via amplification in the lower stratosphere, altering the strength of Hadley circulation in the troposphere[38], with speleothem records indicating that insolation affects monsoon dynamics via Hadley cell and Walker circulation[6]. Sea surface temperature anomalies can extend into the tropical Pacific, modulating ENSO activity thus strengthening the Western Pacific Subtropical High and connecting La Niña with a negative Indian Ocean Dipole during inactive solar phases, increasing rainfall in eastern Asia[37,39].

In large wild herbivores, the primary source of oxygen in body water is plant water, water vapour in air, drinking water, and finally water structurally bound in food[40]. One of the best studied and most highly resolved isotope records from elephant tusks comes from a population in modern Kenya[28]. There, higher $\delta^{18}O$ values were associated with wet seasons, when most of the elephant's water originated from plant water with a high $\delta^{18}O$ signal and less from drinking water with a low $\delta^{18}O$ signature[28]. In our analyses of the Kenyan tusk data, higher $\delta^{18}O$ values are associated with higher solar activity. This observation is consistent with the speleothem $\delta^{18}O$ records of the region: precipitation during the wet season in eastern Africa at interannual to decadal timescales is correlated with sea surface temperatures in the Pacific and Indian Oceans at decadal periodicity[41,42] as well as changes to the Indo-Pacific Walker circulation[43].

In combination, our results suggest that wetter seasons in eastern Africa may be associated with higher solar activity which results in higher sea surface temperatures in the western Indian Ocean and a more positive Indian Ocean Dipole[44]. However, the relationship between solar activity and $\delta^{18}O$ in animal tissues is unlikely to be as straightforward as a direct reflection of precipitation (spectral analysis reveals an 11-year periodicity in the precipitation record associated with the Kenyan tusk but this not significant at the 0.05 level, and the sunspots explain less than 10% of the $\delta^{18}O$ variability). $\delta^{18}O$ in animal tissues is controlled by an animal's physiology, behaviour, diet, and local hydrological

processes[40,45], as well as intraspecific and intraskeletal variation. Moreover, where animals derive a significant proportion of their oxygen from plants, the isotopic composition of soil water, evaporative enrichment in transpiring leaves, and isotopic exchange between oxygen atoms in plant tissues, cells, and organelles will all impact the $\delta^{18}O$ signature of plants[46] and the animals that consume them. Nevertheless, at least some of these plant processes may themselves be impacted by solar activity[47], reinforcing the climate-induced link to solar dynamics controlling $\delta^{18}O$ in water vapour and drinking water.

Cosmogenic radiocarbon (^{14}C) provides one of the most common proxies of solar activity as they are produced by galactic cosmic rays in Earth's atmosphere[47]. Variations in solar activity affect the flux of galactic cosmic ray that reach our atmosphere and thus, ^{14}C production rate[49]. This relationship has been widely used to reconstruct solar activity for past millennia[13,50]. However, stable carbon isotopes have rarely been directly related to sunspot activity even if solar activity is known to impact plant growth and development[51,52], with knock-on effects on fauna[53,54]. Solar cycles at 1100- and 320-year intervals in the coupled $\Delta^{14}C$ and $\delta^{13}C$ record of a South African speleothem suggests that plant community structure is strongly associated with increased irradiance and lower UV-B during periods of increased solar activity[13]. A significant link between stable carbon isotopes in tree ring cellulose and summer sunshine duration has also been reported[47,55]. Higher air temperatures resulting from increased solar activity is hypothesised to reduce stomatal conductance and enhance photosynthetic CO_2 assimilation, thus decreasing the CO_2 concentration in the stomatal cavities of leaves[47]. This lowers the ratio of CO_2 concentration in the stomata relative to ambient CO_2, and because $^{12}CO_2$ is preferentially taken up by plants during photosynthetic carbon assimilation, this change will affect the carbon isotope fractionation leading to less negative $\delta^{13}C$ values in plants during increased solar activity[47]. The impact of higher UV-B on photosynthesis of C3 plants during periods of lower solar cycles could also be considered as UV-B radiation strongly impacts the content and activity of rubisco[56], the enzyme directly responsible for fixing CO_2 in C3 plants[57].

The $\delta^{13}C$ values of the Kenyan tusk follow these predictions, with less negative $\delta^{13}C$ values associated with higher sunspot activity. Applying this finding to our Bangka elephant suggests that sunspot activity peaked at the beginning and end of the formation of tooth BAN19-10, both of which correspond to the lowest $\delta^{18}O$ values, although there is a lag recorded between the trough of $\delta^{18}O$ and the peak of $\delta^{13}C$ (Fig. 2). In Southeast Asia, lower $\delta^{18}O$ values are associated with stronger monsoon conditions[58], suggesting that monsoon intensity in our sample reached a peak during lower sunspot activity, consistent with the model suggested by speleothem data from China and northern Australia[6,37] and with modern systems in the region today[59].

Conclusions

We demonstrate records of solar cycles in animal tissues for the first time, providing a potential new source of high resolution palaeoclimate data where other traditional records such as ice-cores, tree rings, and speleothems are not available. While the preservation and interpretation of climatic data from animal tissues is unlikely to be straightforward or unambiguous, we provide plausible models explaining how $\delta^{18}O$ and $\delta^{13}C$ in elephant enamel may be influenced by solar cycles via their impacts on monsoonal intensities and vegetation changes, respectively. Elephant fossils from Bangka Island, Indonesia are sufficiently well preserved to record annual enamel growth of ~6 mm/year, allowing us to model sinusoidal relationships between $\delta^{18}O$ and $\delta^{13}C$. These records indicate that closed canopy rainforests and a modern monsoonal system, whereby a negative Indian Ocean Dipole coupled with the La Niña phase of ENSO produces higher precipitation, was in place by the early Holocene in Island Southeast Asia.

Materials and Methods

Geological context and fossil specimens

The focus of this study is on several fossil elephant teeth that have been recovered from sedimentary deposits on Bangka Island, east of Sumatra, Indonesia (Fig. 1). Elephant fossils were first reported from near the town of Nibung in Pulau Bangka[60], but the originally collected specimens have not been re-located. They were derived from the Ranggam Formation, a fluviatile sequence consisting of alternating sands, clays, peats, and conglomerates, with well-defined crossbedding, parallel lamination, and graded bedding present[61]. Based on mollusc and foraminifera assemblages, the host formation is thought to be Late Miocene to Early Pleistocene in age[61]. However, ref.[20] indicated that the Ranggam Formation should be considered just one unit of the Ranggam Group, with a second unit, the Residual Gravel, sitting on top of either the Ranggam Formation or pre-Neogene bedrock (Fig. 1). It is this unit, between 0.01 and 2 m thickness, that is argued to hosts terrestrial fossils including elephants as well as most of the alluvial tin[20], the mining of which produced the fossils.

In the eastern parts of the Ranggam Group (Fig. 1), *in situ* outcrops are rare due to long-ongoing and extensive mining of alluvial tin associated with the fossil-bearing sediments[62]; however, an intact outcrop of the Ranggam Formation was located near the town of Nibung and one sediment sample was taken from this location for dosimetry measurements, as part of the Electron Spin Resonance (ESR) dating procedure (BAN19-1; S02.56673°, E106.39872°). No other fossils were observed *in situ*; however, elephant fossils were recovered during hydraulic mining operations at some unknown point prior to June 2019, and in that month were donated to the Institute of Technology, Bandung, where they are registered under their field numbers (BAN19-x). While the exact stratigraphic origin of these fossils is not accessible or likely preserved due to mining activities (it is currently underwater; Fig. 1), local miners were able to indicate the general location of the fossil-bearing beds

(S02.55747°, E106.40331°). The fossils are of presumed late Quaternary age as they were likely recovered from the Residual Gravel unit of the Ranggam Group.

The fossils consist of postcranial elements, four isolated elephant molars, BAN19-8 to BAN19-11, and six elephant molar fragments (BAN19-12), all thought to belong to a single individual[63]. These are described in detail in the SI, with 3D models made using photogrammetry (SI). The complete to mostly complete teeth are all first molars without replication, supporting the suggestion they belong to one individual. From the postcranial elements, fragments of the mid-diaphysis of the humerus, the rib, and the spinous processes of two vertebra were previously analysed histologically[63,64]. Body mass calculations from the humerus provided estimates of ~2500 kg, and histological comparisons with modern *Elephas maximus* indicated more dynamic bone metabolism in the fossil elephant. Radiocarbon dating was attempted at the Australian National University Radiocarbon Laboratory, but the specimens did not preserve sufficient collagen for analysis.

Direct U-series and ESR dating

Tooth BAN19-11 was selected for dating as it was the most broken but mostly complete tooth. Sampling was performed on one of the biggest enamel lamellae at the centre of the tooth, from which two enamel pieces (#11A and #11C) with adjacent dentine on both sides were extracted with dental drill (Figure S1). While subsample #11A is located close to the occlusal surface, #11C is positioned more inside the tooth, about 2 cm from the (lateral and occlusal) edges of the enamel. The latter subsample was analysed for combined U-series/ESR dating, while the former was U-series analysed to evaluate the spatial variability of U-series elements in the tooth. The ESR dose evaluation was performed at the Centro Nacional de Investigación sobre la Evolución Humana (CENIEH), Spain, following the multiple aliquot additive dose (MAAD) method based on enamel powder. Solution U-series analyses of powdered dental tissues were carried out using a Nu Plasma multi-collector inductively-coupled plasma mass spectrometer (MC-ICP-MS) in the Radiogenic Isotope Facility at The University of Queensland, Brisbane, Australia.

The sediment attached to fossil specimens BAN19-10 and BAN19-11 was collected for dose rate evaluation. Three sediment samples (Sed #10A, #10B and #10C) were obtained from BAN19-10 (Figure S1), while one sediment sample was collected from the occlusal surface of BAN19-11 (Sed #11). Sediment texture and facies of Sed #11 is similar to that of sample Sed #10C (Table S1). One additional sediment sample (BAN19-1) was analysed based on hypothesised alternative provenance (see above). Combined U-series/ESR age calculations carried out for #11C and associated data inputs and outputs are given in Table S5. Errors are 1σ unless specified otherwise. Sampling preparation and dose rate evaluation methods are detailed in the SI.

Histology

BAN19-12 (Figures S4-5) was used to prepare histology thin sections used to estimate the rate of enamel extension following the method employed by ref.[22]. We followed standard palaeohistology preparation methods[65] and protocols developed in the Histology Laboratory at the Australian National University[66,67]. Full details are provided in the SI.

Serial isotope sampling

A diamond burr drill bit was used to sample an individual lamella per tooth, with samples taken from the base to the crown. After drilling, the molars were again photographed and the distance between the midpoint of each drill point calculated using FIJI/ ImageJ software[68]. Twenty-two samples were drilled from lamella 9 of BAN19-8, with an average distance of 5 mm between sample points; 19 samples were drilled from lamella 6 of BAN19-9, average distance 5.2 mm; 20 samples from BAN19-10 lamella 7, average distance 4.7 mm; and 15 samples from BAN19-11, likely lamella 6 or 7, average distance between samples 5.1 mm.

Carbon and oxygen isotope ($\delta^{13}C$ and $\delta^{18}O$) analysis was undertaken on powdered enamel following procedures outlined in ref.[69]. Organics were removed from the enamel powder using 30% H_2O_2 and 0.1 N acetic acid. The inorganic fraction of the enamel samples was measured using a ThermoFinnigan DeltaPlus XP mass spectrometer at the University of Rochester's Stable Isotope Ratios in the Environment Analytical Laboratory. Carbon and oxygen isotopes are standardised to Vienna Pee-Dee Belemnite and reported in permil (‰). Where possible, we ran repeat analyses and discarded the results with the highest standard deviation across both oxygen and carbon isotope ratios. Statistical analysis of isotope values was undertaken using PAST v2.17c[70].

Acknowledgements

We are grateful to María Jesús Alonso Escarza and Javier Iglesias Cibanal, CENIEH, for technical support around the analytical procedure**.**

Funding

This investigation is funded by the ARC Discovery projects DP230101273, FT160100450, FT150100215, FT240100030, and DE190100068. MD's investigations are supported by Spanish Grant GBCHRON PID2024-155126NB-I00 funded by MICIU/AEI/10.13039/501100011033 and by ERDF/EU. MD also receives support from the HUMAN ORGINS Cluster of Excellence funded by the Deutsche Forschungsgemeinschaft (DFG, German Research Foundation) under Germany's Excellence Strategy - EXC 3101/01 - Project number 533763844.

References

[1]Scerri, E.M., Roberts, P., Yoshi Maezumi, S. & Malhi, Y. Tropical forests in the deep human past. Philosophical Transactions of the Royal Society B: Biological Sciences 377, 1849 (2022).

[2]Freidline, S.E. et al. Early presence of Homo sapiens in southeast Asia by 86–68 kyr at Tam Pà Ling, Northern Laos. Nature Communications 14, 3193 (2023).

[3]Louys, J. et al. Speleological and environmental history of Lida Ajer cave, western Sumatra. Philosophical Transactions of the Royal Society B 377, 20200494 (2022).

[4]Louys, J. & Roberts, P. Environmental drivers of megafauna and hominin extinction in Southeast Asia. Nature 586, 402–406 (2020).

[5]Hamilton, R. et al. Forest mosaics, not savanna corridors, dominated in Southeast Asia during the Last Glacial Maximum. Proceedings of the National Academy of Sciences 121, e2311280120 (2024).

[6]Eroglu, D. et al. See–saw relationship of the Holocene East Asian–Australian summer monsoon. Nature Communications 7, 12929 (2016).

[7]Claud, C., Duchiron, B. & Terray, P. On associations between the 11-year solar cycle and the Indian Summer Monsoon system. Journal of Geophysical Research: Atmospheres 113 (2008).

[8]Roberts, P., Hamilton, R. & Piperno, D.R. Tropical forests as key sites of the "Anthropocene": Past and present perspectives. Proceedings of the National Academy of Sciences 118, e2109243118 (2021).

[9]Louys, J. & Meijaard, E. Palaeoecology of Southeast Asian megafauna-bearing sites from the Pleistocene and a review of environmental changes in the region. Journal of Biogeography 37, 1432–1449 (2010).

[10]Suraprasit, K. et al. Late Pleistocene human paleoecology in the highland savanna ecosystem of mainland Southeast Asia. Scientific Reports 11, 16756 (2021).

[11]Bacon, A.M. et al. A multi-proxy approach to exploring Homo sapiens' arrival, environments and adaptations in Southeast Asia. Scientific Reports 11, 21080 (2021).

[12]Duan, F. et al. Evidence for solar cycles in a late Holocene speleothem record from Dongge Cave, China. Scientific Reports 4, 5159 (2014).

[13]Woodborne, S., Mélice, J.L. & Scholes, R.J. Long-term sunspot forcing of savanna structure inferred from carbon and oxygen isotopes. Geophysical Research Letters 35 (2008).

[14]Gagan, M.K. et al. Onset of summer aridification and the decline of Homo floresiensis at Liang Bua 61,000 years ago. Communications Earth & Environment 6, 992 (2025).

[15]Carolin, S.A. et al. Varied response of western Pacific hydrology to climate forcings over the last glacial period. Science 340, 1564–1566 (2013).

[16]Carolin, S.A. et al. Northern Borneo stalagmite records reveal West Pacific hydroclimate across MIS 5 and 6. Earth and Planetary Science Letters 439, 182–193 (2016).

[17]Meckler, A.N. et al. Interglacial hydroclimate in the tropical West Pacific through the Late Pleistocene. Science 336, 1301–1304 (2012).

[18]Griffiths, M.L. et al. Increasing Australian–Indonesian monsoon rainfall linked to early Holocene sea-level rise. Nature Geoscience 2, 636–639 (2009).

[19]Partin, J.W. et al. Millennial-scale trends in west Pacific warm pool hydrology since the Last Glacial Maximum. Nature 449, 452–455 (2007).

[20]Ko Ko, U. Preliminary synthesis of the geology of Bangka Island, Indonesia. GEOSEA V Proceedings Vol. II of the Geological Society of Malaysia, Bulletin 20, 81–96.

[21]Christiansen, P. Body size in proboscideans, with notes on elephant metabolism. Zoological Journal of the Linnean Society 140, 523–549 (2004).

[22]Metcalfe, J.Z. & Longstaffe, F.J. Mammoth tooth enamel growth rates inferred from stable isotope analysis and histology. Quaternary Research 77, 424–432 (2012).

[23]Dirks, W., Bromage, T.G. & Agenbroad, L.D. The duration and rate of molar plate formation in Palaeoloxodon cypriotes and Mammuthus columbi from dental histology. Quaternary International 255, 79–85 (2012).

[24]Christiansen, P. Body size in proboscideans, with notes on elephant metabolism. Zoological Journal of the Linnean Society 140, 523-549 (2004).

[25]van der Geer, A.A. et al. The effect of area and isolation on insular dwarf proboscideans. Journal of Biogeography 43, 1656–1666 (2016).

[26]Ma Jiao et al. A preliminary study of serial stable isotope analysis tracks foraging ecology of fossil Asian elephants in South China. Vertebrata PalAsiatica 57, 225 (2019).

[27]Hathaway, D.H. The solar cycle. Living Reviews in Solar Physics 12, 4 (2015).

[28]Uno, K.T. et al. High-resolution stable isotope profiles of modern elephant tusk dentin and tail hair from Kenya. Palaeogeography, Palaeoclimatology, Palaeoecology 559, 109962 (2020).

[29]WDC-SILSO. Royal Observatory of Belgium, Brussels (2025).

[30]Kershaw, P. & Van Der Kaars, S. Pollen records, late Pleistocene Australia and New Zealand. In Encyclopedia of Quaternary Science, 2613–2623 (Elsevier, 2006).

[31]Gallagher, S.J. et al. Cenozoic history of the Australian Monsoon. Progress in Earth and Planetary Science 11, 1–32 (2024).

[32]Denniston, R.F. et al. A stalagmite record of Holocene Indonesian–Australian summer monsoon variability. Quaternary Science Reviews 78, 155–168 (2013).

[33]Wang, Y. et al. The Holocene Asian monsoon: links to solar changes and North Atlantic climate. Science 308, 854–857 (2005).

[34]Bond, G. et al. Persistent solar influence on North Atlantic climate during the Holocene. Science 294, 2130–2136 (2001).

[35]Fleitmann, D. et al. Holocene forcing of the Indian monsoon recorded in a stalagmite from southern Oman. Science 300, 1737–1739 (2003).

[36]Wang, Z. et al. A high-resolution stalagmite record from Luoshui Cave, Central China over the past 23.5 kyr. Quaternary Science Reviews 282, 107443 (2022).

[37]Chen, X. et al. New insights into potential effects of solar activity on modern speleothems. Journal of Hydrology 625, 130114 (2023).

[38]Lin, Y.-F. et al. Footprint of the 11-year solar cycle in Pacific SSTs. Geophysical Research Letters 48, e2020GL091369 (2021).

[39]Kodera, K., Coughlin, K. & Arakawa, O. Modulation of Pacific–Indian Ocean variability by solar cycle. Geophysical Research Letters 34 (2007).

[40]Kohn, M.J. Predicting animal d18O: accounting for diet and physiological adaptation. Geochimica et Cosmochimica Acta 60 (1996).

[41]Nicholson, S.E. Climate variability of rainfall over eastern Africa. Reviews of Geophysics 55, 590–635 (2017).

[42]Omondi, P. et al. Decadal rainfall variability modes in East Africa. Journal of Hydrology 464–465, 140–156 (2012).

[43]Liebmann, B. et al. Understanding eastern Horn of Africa rainfall variability. Journal of Climate 27, 8630–8645 (2014).

[44]Zheng, Y. et al. Indian Ocean dipole impacts on Eastern African rains. Earth's Future 13, e2024EF005219 (2025).

[45]Fricke, H.C. et al. Intra-tooth δ18O variations and climate seasonality. Geochimica et Cosmochimica Acta 62, 1839–1850 (1998).

[46]Barbour, M.M. Stable oxygen isotope composition of plant tissue. Functional Plant Biology 34, 83–94 (2007).

[47]Churakova (Sidorova), O.V. et al. Tree rings indicate millennia sunshine changes. Science of the Total Environment 927, 172042 (2024).

[48]Usoskin, I.G. A history of solar activity over millennia. Living Reviews in Solar Physics 20, 2 (2023).

[49]Gray, L.J. et al. Solar influences on climate. Reviews of Geophysics 48 (2010).

[50]Wu, C.J. et al. Solar irradiance reconstruction over 9000 years. Astronomy & Astrophysics 620, A120 (2018).

[51]Mironov, V.L. Solar activity effects on plant growth. Physiologia Plantarum 174, e13733 (2022).

[52]Montefalcone, M. et al. Seagrass flowering and solar activity. Mediterranean Marine Science 416–423 (2013).

[53]Selås, V. et al. Sunspot activity and forest moth outbreaks. Proceedings of the Royal Society B 271, 1897–1901 (2004).

[54]Selås, V. UV-B plant stress and hare cycles. Population Ecology 48, 71–77 (2006).

[55]Loader, N.J. et al. Carbon isotopes and sunshine reconstruction. Quaternary Science Reviews 62, 97–113 (2013).

[56]Lidon, F.J. et al. Impact of UV-B on photosynthesis. Emirates Journal of Food Agriculture 24, 546–556 (2012).

[57]O'Leary, M.H. Carbon isotopes in photosynthesis. Bioscience 38, 328–336 (1988).

[58]Ziegler, S. et al. Isotope variability in elephant ivory. Biological Conservation 197, 154–163 (2016).

[59]Nur'utami, M.N. & Hidayat, R. IOD and ENSO effects on Indonesian rainfall. Procedia Environmental Sciences 33, 196–203 (2016).

[60]Martin, K. Ueberreste vorweltlicher Proboscidier von Java und Banka. Beiträge zur Geologie Ost-Asiens und Australiens 4, 1–24 (1884).

[61]Margono, U., Supandjono, R.J.B. & Partoyo. Peta Geologi Lembar Bangka Selatan. Bandung (1995).

[62]Louys, J. et al. Palaeontological surveys in Central Sumatra and Bangka. Berita Sedimentologi 47, 50–56 (2021).

[63]Basilia, P. et al. Bone histology in a fossil elephant from Bangka. Historical Biology 35, 1356–1367 (2023).

[64]Basilia, P. et al. Super osteons in fossil Asian elephant bone. In Quaternary Palaeontology and Archaeology of Sumatra (2024).

[65]Padian, K. & Lamm, E.T. Bone histology of fossil tetrapods. (University of California Press, 2013).

[66]Campbell, B. et al. Crocodile tooth histology from Chinchilla. Proceedings of the Royal Society of Queensland 129, 37–46 (2021).

[67]Snoddy, A.M.E. et al. Image analysis of interglobular dentine. American Journal of Physical Anthropology 174, 144–148 (2021).

[68]Schindelin, J. et al. The ImageJ ecosystem. Molecular Reproduction and Development 82, 518–529 (2015).

[69]Louys, J. et al. Geochronology and palaeoenvironments of Sibrambang and Djambu caves. In Terra Australis 99–120 (2024).

[70]Hammer, Ø., Harper, D.A. & Ryan, P.D. PAST: Paleontological statistics software package. Palaeontologia Electronica 4, 9 (2001).

Extended Tables

Extended Table 1. ESR age sensitivity tests performed by varying the gamma and cosmic dose rates. See explanations in the main text and SI.

Scenario	Gamma dose rate	Cosmic dose rate	ESR age (ka)
1	Average radioelement concentrations	depth = 5 m	7.83 ± 1.19
2	#10B	depth = 5 m	8.71 ± 1.31
3	#10C	depth = 5 m	12.6 ± 1.87
4	#11SED	depth = 5 m	3.68 ± 0.56
5	BAN19-1	depth = 5 m	22.0 ± 3.24
6	Average radioelement concentrations	depth = 1 m	7.67 ± 1.14
7	Average radioelement concentrations	depth = 40 m	8.06 ± 1.25

458

459 **Extended Table 2**. Descriptive statistics of the averaged measurements of d – width of
460 enamel cross-striations, D – the angle between EDJ and Retzius lines, I – the angle between
461 EDJ and enamel rods (I), c (extension rate), and an estimate in mm per year. (SD: standard
462 deviation).

Statistics	d (µm)	D (degree)	I (degree)	c (µm/day)	Enamel extension-rate estimate (mm/yr)
Mean	2.85	6.32	46 ± 3.43	16.490	6.018
Range (Min)	2.2	5.76	40.49	13	4.786
Range (Max)	3.3	6.86	49.77	18.5	6.751
Range (Median)	2.9	6.43	46.38	16.823	6.14
SD	0.28	0.334	3.43	1.56	0.569

463

464 **Extended Table 3**. Comparison of enamel histology measurements collected in this study for
465 *E. maximus* with those from published sources for *M. columbi* and *P. cypriotes.* np: not
466 provided.

Comparative data	***M. columbi***[22]	***M. columbi***[23]	***E. maximus*** (this study)	***P. cypriotes***[23]
Estimated body mass average	6630 kg[24]		2567 kg	200 kg[25]
Prism formation/day (d) (cross-striation width)	4.4 ± 0.6 µm/day	3.5 ± 0.5 µm/day	2.86 ± 0.28 µm/day	3.2 ± 0.6 µm/day
Angle between Striae of Retzius and EDJ (D)	6.1 ± 0.8°	np	6.32 ± 0.33°	np
Angle between enamel prisms and EDJ (I)	44.9 ± 5.4°	np	46 ± 3.43°	np
Calculated enamel extension rates (c)	14 to 43 µm/day	32.3 to 62.5 µm/day	13 to 18.5 µm/day	12 to 26.6 µm/day
Mean Calculated enamel extension rates (c)	26 µm/day	np	16.5 µm/day	np
Enamel extension-rate estimate (mm/yr)	5.2 to 15.5 mm/yr	np	4.79 - 6.75 mm/yr	np
Age estimates	3-5 yrs*	5-10 yrs	unknown	3-6 yrs
Mean Enamel extension-rate estimate (mm/yr)	9.5 mm/yr	11.8 to 13.8 mm/yr	6 mm/yr	4.38 to 8.5 mm/yr

*Based on ref[23] age estimates from enamel extension rates.

Extended Table 4. Spectral analysis for each Bangka elephant tooth.

Tooth	$\delta^{13}C$ frequency (mm along tooth)	Maximum power ($\alpha = 0.05$)	$\delta^{18}O$ frequency (mm along tooth)	Maximum power ($\alpha = 0.05$)
BAN19-8	12.7	3.72 (6.76)	13.1	2.74 (6.76)
BAN19-9	107.7	4.88 (6.56)	20.4	2.27 (5.56)
BAN19-10	96.1	4.86 (6.44)	67.2	4.41 (6.44)
BAN19-11	28.5	2.04 (5.74)	20.8	1.98 (5.74)

Extended Table 5. Periodicity analyses corresponding to frequencies from spectral analyses of V 22700.02, V22700.03 (ref.[25]) or the Bangka elephant teeth.

Tooth	92.8 mm $\delta^{13}C$ frequency of V 22700.02 (p/AIC)	$\delta^{13}C$ frequency from spectral analysis (p/AIC)	74.2 mm $\delta^{18}O$ frequency of V 22700.02 (p/AIC)	41.0 mm $\delta^{18}O$ frequency of V 22700.03 (p/AIC)	$\delta^{18}O$ frequency from spectral analysis (p/AIC) (p/AIC)
BAN19-8	0.92/na	0.12/na	0.56/na	0.16/na	0.09/na
BAN19-9	0.00/6.96	0.00/6.72	0.10/na	0.87/na	0.09/na
BAN19-10	0.00/5.69	0.00/5.67	0.00/7.70	0.21/na	0.01/9.10
BAN19-11	0.20/na	0.31/na	0.31/na	0.71/na	0.39/na

Figures

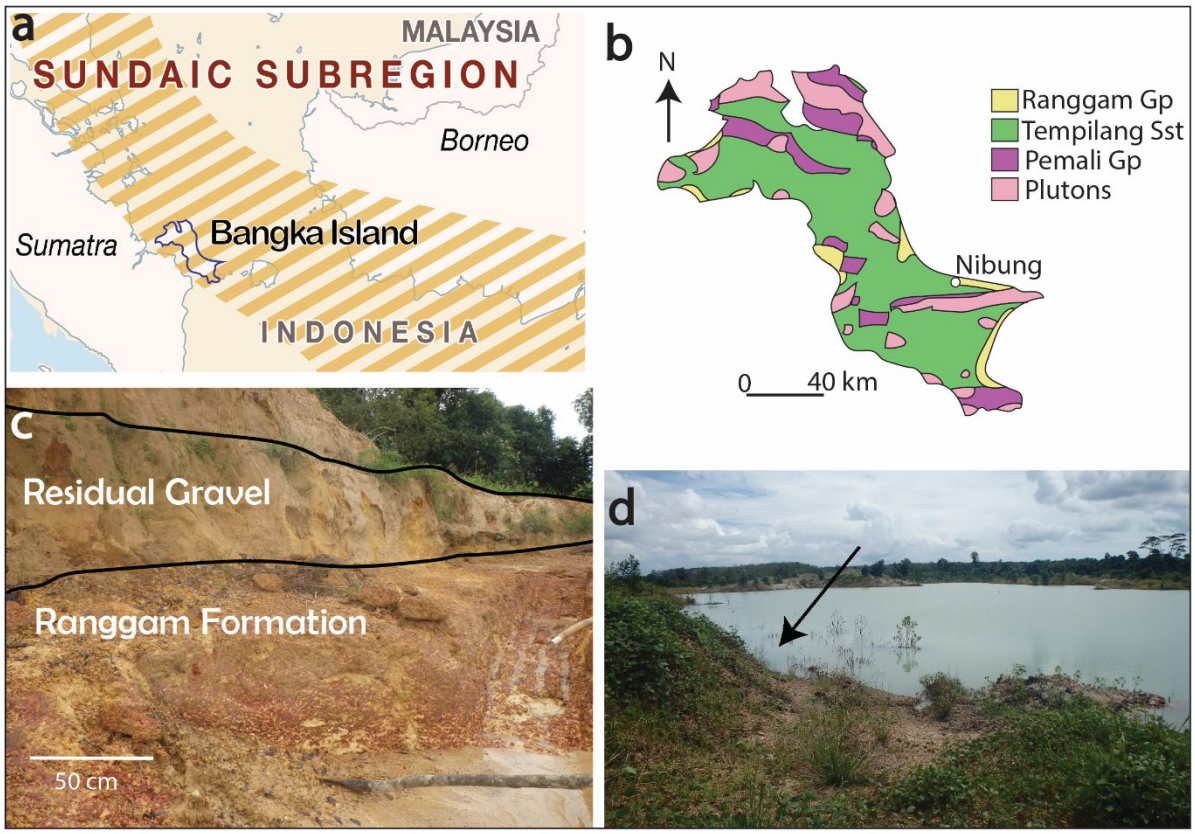

Figure 1. Location map of Bangka Island and source of the elephant fossils: (a) regional map showing Bangka Island relative to Sumatra and Borneo and the maximum extent of the Sunda Shelf (light tan shading), with the 'savannah corridor' marked in dark tan diagonal lines (after ref.[4]); (b) geological map of Bangka Island showing major formations (after refs[20,61]); (c) *in situ* outcrop showing the Residual Gravel and Ranggam Formation units of the Ranggam Group near Nibung; (d) approximate location of the elephant fossils examined here.

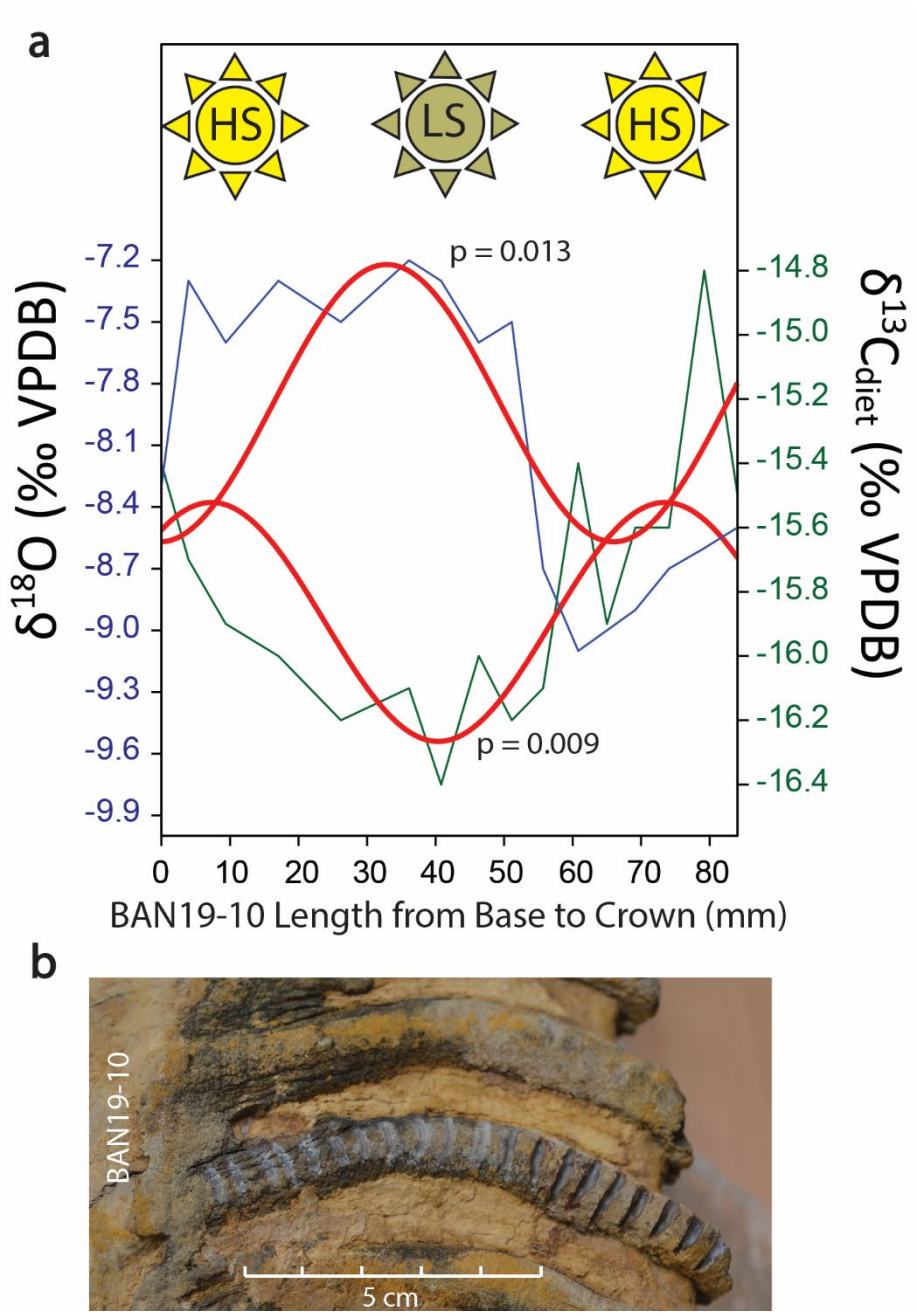

481

482 Figure 2. (a) Sinusoidal models of BAN19-10 $\delta^{18}O$ (left y-axis) and $\delta^{13}C$ (right y-axis)
483 values, corresponding to frequencies from spectral analysis of the isotope values; (b) the
484 drilled tooth. HS refers to high solar activity, LS low solar activity.

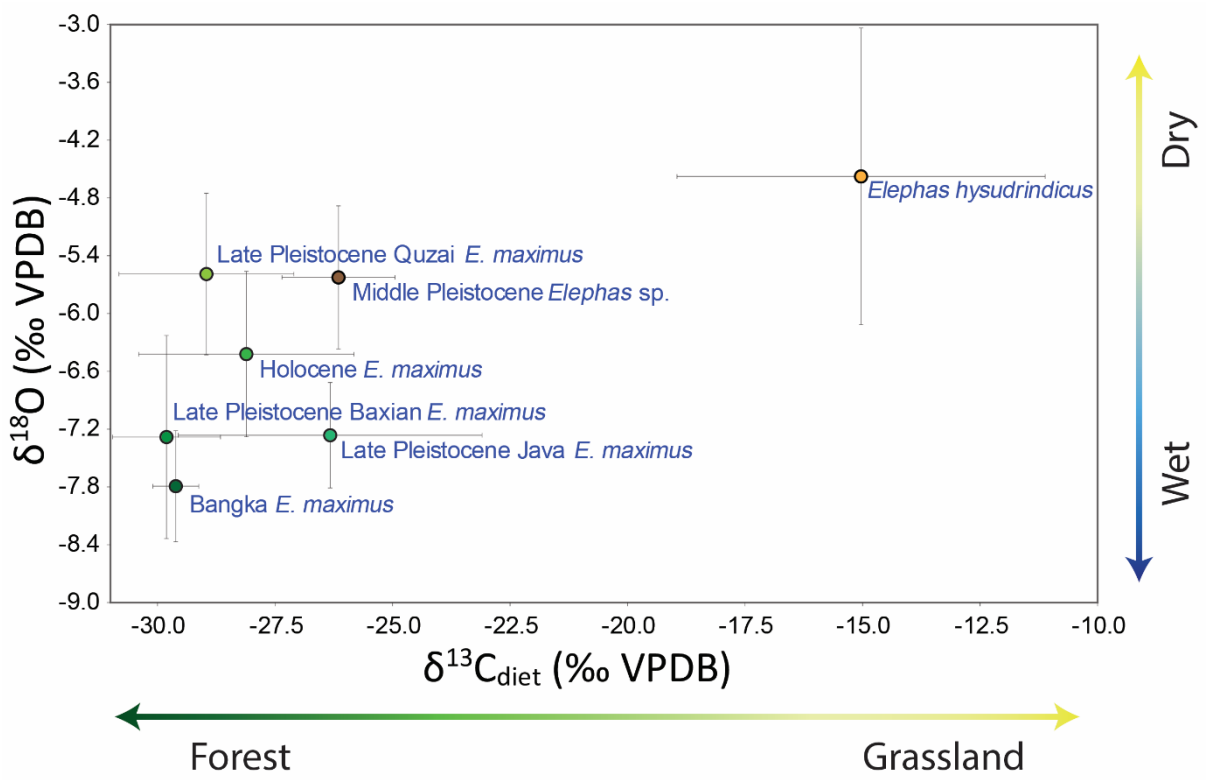

485

486 **Extended Figure 1.** Quaternary proboscidean $\delta^{18}O$ and $\delta^{13}C$ isotope records and their

487 corresponding climatic and environmental interpretations. Data from refs[4,26].

Supplementary Information for Decadal-scale climate cycles preserved in megaherbivore dental tissues in tropical Asia

Louys, Julien[1*]; Miszkiewicz, Justyna J.[2,3]; Higgins, Penny[4], Mathieu Duval[1,5,6], Zaim, Yahdi[7,8]; Puspaningrum, Mika R.[7]; Rizal; Yan[7]; Aswan[7]; Rowe, Joshua[1]; Basilia, Pauline[1]; Loïc Martin[9]; Breitenbach, Sebastian F.M.[10]; Price, Gilbert J.[11]

[1]Australian Research Centre for Human Evolution, Griffith University, Brisbane, Australia

[2]School of Social Science, The University of Queensland, Brisbane, Australia

[3]Earth, Life, Time Group, Naturalis Biodiversity Center, Leiden, The Netherlands

[4] EPOCH Isotopes, 6606 E Townline Rd, Williamson, NY 14589, USA

[5]Centro Nacional de Investigación sobre la Evolución Humana (CENIEH), Paseo Sierra de Atapuerca 3, 09002 Burgos, España

[6]Palaeoscience Labs, Department of Archaeology and History, La Trobe University, Melbourne, Australia

[7]Paleontology and Quaternary Geology Research Group, Faculty of Earth Sciences and Technology, Institut Teknologi Bandung, Bandung, Indonesia

[8]Department of Geology, Institute of Technology Sumatera (ITERA), Lampung, Indonesia

[9]Institute for Geology, University of Innsbruck, Innsbruck, Austria

[10]School of Geography and Natural Sciences, Northumbria University, Newcastle Upon Tyne, UK

[11]School of the Environment, The University of Queensland, Brisbane, Australia

S1. Fossil Molar Descriptions

The fossils from Bangka analysed consisted of five molar remains, of which four were isolated M1s, and very likely came from a single individual (BAN19-8, BAN19-9, BAN19-10 and BAN19-11). BAN19-8 is a relatively complete upper left first molar (M^1) with a preserved length of 220 mm and crown height of 159 mm. When viewed from the side with the occlusal surface in a horizontal position, the lamellae appear to be folded in a sinusoidal way, a feature common in high-crowned *Elephas* molars. It preserves at least -11½ lamellae, the half posterior lamellae and 11 are unworn, the lamellae 10 up to 3 are worn gradually with buccal and lingual parts still intact. The lamellae 2 and 1 are almost completely worn away, leaving only a small amount of occlusal remnant, while the buccal and lingual portions have been worn away. The widest part is positioned on lamellae 4, in the middle of the lamellar height with a maximum width of 84.1 mm and minimum of 17.7 mm on the posterior half lamellae.

Sample BAN19-9 is a 176 mm long lower left first molar (M_1), with a crown height of 107 mm and 8½ preserved lamellae. Only the posterior half lamellae and lamella 8 are unworn while lamellas 7 to 1 show increasing wear, ranging from slightly to moderately worn. The widest part is on the lamella 3 with maximum width of 73 mm, and the minimum width on the posterior half lamellae measured at 17.4 mm. Sample BAN19-10 is a right lower M_1 with ten preserved lamellae of 220 mm maximum length and a crown height of 113 mm. Only the lamellae 10 is unworn, while lamella 9 to 1 are increasingly worn from slightly to almost fully worn. Lamella 1 has only a small amount of posterior enamel remaining in the centre, while the buccal part of lamella 2 is worn. Maximum and minimum lamellar width measuring 73.5 mm (at lamellae 5) and 37 mm (at lamellae 10). The partial upper right M^1 BAN19-11 preserves 6 lamellae, with maximum length of 86 mm and a crown height of 132 mm. Lamella 6 is slightly worn and consists of only half of the anterior enamel. As it moves toward the anterior, the lamellae become more worn, with the anterior most lamellae remaining only about a quarter of its height. In terms of size and wear, the six lamellae in BAN19-11 are paired with lamellae 4-9 in BAN19-8. Of the six fragments associated with BAN19-12 only the anterior portion of a molar preserving two lamellae and a separated partial lamellar can be confidently identified. Maximum length preserved is 60 mm and crown height is 34 mm.

S2. 3D Photogrammetry

Three-dimensional digital models of the isolated fossil elephant teeth were generated using close-range photogrammetry. Specimens were photographed using a Nikon DSLR D5200 camera mounted on a fixed tripod to maintain consistent camera geometry throughout image acquisition. Each tooth was placed on a manual turntable and imaged through a full 360° rotation, with photographs taken at approximately 20° intervals. To ensure complete surface coverage and to minimise occluded areas, images were collected at three vertical camera heights (low, mid, and high angles) for each rotational position. This procedure was repeated with the specimen inverted to capture the opposite surface, resulting in comprehensive coverage of both occlusal and basal surfaces. This approach allows for the rendering of a single 3D model for each tooth that captures all surfaces of the specimen. In total, approximately 108 overlapping photographs were acquired per specimen.

All images were processed in Agisoft Metashape Professional (Agisoft LLC, St. Petersburg, Russia). Photographs were first aligned using a high-accuracy setting to generate a sparse point cloud. Erroneous tie points were removed manually where necessary before generating a dense point cloud using the high-quality reconstruction option. A polygon mesh was then built from the dense cloud and textured using the original photographs to produce a photorealistic 3D surface model. Final models were inspected for completeness and artefacts, and minor imperfections were corrected using the built-in cleaning tools in Metashape. Resulting meshes were exported in standard formats (i.e., OBJ and associated material files) for measurement, visualisation, and archiving. These are available online through Sketchfab (https://sketchfab.com/).

S3. Direct U-series and ESR dating

S3.1 Sample preparation

The different tissues associated with tooth fragments #11A and #11C were mechanically separated and cleaned to avoid contamination from other tissues or sediment. In particular, the inner and outer surfaces of the piece of enamel of #11C were removed with a dental drill to eliminate the sample volume that received an external alpha dose. The initial and removed enamel thicknesses were measured with a micrometer. The clean enamel and dentine subsamples of #11A and #11 C were manually ground with an agate mortar and pestle and sieved using <200 μm mesh size to obtain homogenous powders for ESR and U-series analyses.

S3.2 ESR dose evaluation

The ESR dose evaluation was performed at the Centro Nacional de Investigación sobre la Evolución Humana (CENIEH), Spain. Dose evaluation used the multiple aliquot additive dose (MAAD) method. The enamel powder of #11C was split into eleven aliquots and irradiated with a Gammacell 1000 Cs-137 gamma source (dose rate = 6.27 ± 0.14 Gy/min) to the following doses: 0, 49.0, 98.1, 147.0, 196.0, 294.1, 392.1, 588.0, 784.0, 980.0 and 1960.0 Gy.

ESR measurements were carried out at room temperature with an EMXmicro 6/1 Bruker ESR spectrometer coupled to a standard rectangular ER 4102ST cavity. The following procedure was used to minimise the analytical uncertainties: (i) all aliquots of a given sample were carefully weighted into their corresponding tubes and a variation of <1 mg was tolerated between aliquots (average weight per aliquot ~20 mg); (ii) ESR measurements were performed using a Teflon sample tube holder inserted from the bottom of the cavity to ensure that the vertical position of the tubes remains exactly the same for all aliquots. The following acquisition parameters were used: 1-60 scans depending on the aliquot considered, 1 mW microwave power, 1024 points resolution, 15 mT sweep width, 100 kHz modulation frequency, 0.1 mT modulation amplitude, 20 ms conversion time and 5 ms time constant. All aliquots of #11C were measured within <1 h. This procedure was repeated two times over successive days without removing the enamel from the ESR tubes between measurements to evaluate measurement and equivalent dose (D_E) precisions.

The ESR intensities were extracted from T1-B2 peak-to-peak amplitudes of the ESR signal (Grün, 2000a) after a cubic baseline correction and noise subtraction following Arnold et al. (2024) and normalised to the corresponding number of scans and aliquot mass. DE values were obtained by fitting a single saturating exponential (SSE) through the mean ESR intensities derived from the repeated measurements. Fitting was performed with Microcal OriginPro 9.1 software, which is based on the Levenberg-Marquardt algorithm by chi-square minimisation. Data were weighted by the inverse of the squared ESR intensity ($1/I^2$) (Grün and Brumby, 1994; Duval and Grün, 2016). The ESR dose response curve (DRC) is displayed in Figure S2, while numerical fitting results are given in Table S2.

S3.3 Solution U-series analyses

Powdered enamel and dentine samples of #11A and #11C were weighed then spiked using a 229Th-233U tracer before being digested in concentrated HNO3. The solutions were treated with H2O2 to remove trace organics, with U and Th then separated using conventional column chemistry techniques described in Clark et al. (2014). Both U and Th were collected into the same pre-cleaned test tube using 3 ml of 2% HNO3 mixed with a trace amount of HF. U-Th isotope ratios were then measured using a Nu Plasma multi-collector inductively-coupled plasma mass spectrometer (MC-ICP-MS) in the Radiogenic Isotope Facility at The University of Queensland, Brisbane, Australia, following analytical protocols described in Zhao et al. (2009), Price et al. (2013) and Clark et al. (2014). Analytical results are given in Table S3.

S3.4 Gamma dose rate modelling

Given its large size, the elephant tooth is expected to significantly contribute to the gamma dose rate by dosing and shielding the enamel layer (unlike horse or bovid teeth; see Grün, 1992), and a proper evaluation of the gamma attenuation and self-absorption factors was deemed necessary. For this purpose, a 3D geochronological model of BAN19-11 was created (Figure S3). By considering the size of the tooth, a succession of dentine (70 mm thick) and enamel (3 mm thick) layers with assumed homogenous spatial distribution of uranium concentrations (dental tissues are typically free of Th and K) and equilibrium in the 238U decay chain, were modelled, with the position of subsamples #11A and #11C integrated. Gamma dose rate simulations were performed using DosiVox and GEANT4 code (Martin et al., 2015). Results are summarized in Table S4.

S3.5 Combined U-series/ESR age calculations

Because the tooth's original location is unknown, no in situ evaluation of the natural radioactivity of the surrounding environment was possible, and the gamma dose rate must be derived from the laboratory analysis of sediment samples collected from the fossil specimens and in the field. U, Th and K contents were obtained from the ICP-OES/MS analysis of the dry raw sediment (previously powdered and homogenized) following a four-acid digest preparation procedure (Table S1).

The following parameters were used for the dose rate calculations: an alpha efficiency of 0.13±0.02 (Grün and Katzenberger-Apel, 1994), Monte-Carlo beta attenuation factors from Marsh (1999), dose-rate conversion factors from Guérin et al. (2011), an estimated water content of 0 and 5±3 wt.% in enamel and dentine, respectively. Although the supposed locality of origin of the fossils is currently underwater, these modern conditions are most likely the results of the intense mining activities and may not be regarded as being representative of the burial history of the fossil specimen. Consequently, a long-term water content value of 20 ± 10 % (% dry weight) was initially assumed. The large associated error is meant to encompass the fluctuations of the water content over time.

The geomorphology of the local area from where the fossil teeth likely originate suggests that the apparent depth for the fossil horizon does not exceed 5 m. Consequently, the cosmic dose rate evaluation was based on a depth of 5 ± 3 m, while the large relative error (60%) is chosen to encompass the non-negligible uncertainty on this estimate. A sample geometry dentine/enamel/dentine was considered for the beta dose rate attenuations.

Combined U-series/ESR age calculations for #11C were performed with DATA (Grün et al., 2009) and USESR (Shao et al., 2014), which are DOS-based and Matlab-based programs using the US, CSUS and AU models defined by Grün et al. (1988), Grün (2000b) and Shao et al., (2012), respectively. Data inputs and outputs are given in Table S5.

S3.6 Results

S3.6.1 Solution U-series dating results

Apparent U-series ages of dental tissues associated with samples #11A and #11C range from ~30 to ~320 ka (Table S2). The enamel of #11C displays a significantly older age estimate than other tissues, suggesting that it may reflect uranium leaching overprinting and not the 'true' age of the tooth. While the apparent U-series estimate of ~320 ka should most likely be disregarded as a reliable age constraint, this leaching overprint is, however, unlikely to

significantly impact the combined U-series/ESR age calculation given the very small uranium concentration measured in the enamel (<0.1 ppm).

The dentine on each side of the enamel layer (inner and outer sides are indicated in Figure S1) associated with either #11A or #11C displays very distinct U-series data: on the inner side, apparent U-series ages range from ~30 to ~40 ka, and uranium concentrations are between 2 and 20 ppm, whereas the outer dentine shows older apparent ages of ~55-60 ka and very low uranium concentration (0.05 ppm). These data show the spatial heterogeneity of the U-series data within the elephant tooth, an issue that has been highlighted on several occasions in the past (e.g. Grün and Invernati, 1985; Bahain et al., 1992).

Interestingly, since inner dentine #11A is positioned much closer to the occlusal surface than #11C, the younger U-series data (30 vs 40 ka) and higher uranium concentrations (20 vs 2 ppm) may suggest a recent uranium uptake overprint coming from the occlusal surface. A similar observation was reported by Grün and Invernati (1985). This is apparently happening only on one (the inner) side of the enamel, while on the other, the outer dentine from #11A and #11C display similar U-series data. Alternatively, it cannot be excluded that the dentine layer positioned on the so-called inner side may have experienced a more recent uranium uptake process as indicated by the younger ages and significantly higher uranium concentrations. In other words, the dentine domains with lower uranium concentration show the oldest apparent U-series ages, which might reflect an older uranium uptake process. These latter domains are would be interpreted as providing a reliable minimum age constraint of ~56 to ~61 ka for the fossil tooth, but only independently of any uranium leaching revealed through combined interpretation of the U-series data with ESR results.

S3.6.2 ESR data

ESR measurements carried out with ~20 mg aliquots returned a minimum signal-to noise (S/N) ratio of 7.4 from the natural aliquot, while the spectra of the least irradiated aliquots showed a non-horizontal baseline, which may induce a considerable overestimation of the T1B2 ESR intensities if not considered. Consequently, all ESR intensities were derived after a baseline correction and subtraction of the high-frequency random noise. The ESR DRC is graphically displayed in Figure S1, while the numerical fitting results are given in Table S3. Two repeated ESR measurements were performed, showing limited variation in the ESR intensities (0.1%) and in the D_E estimates (7.4%). DRC fitting over the full dose range (D_{max} = 1960 Gy) yields a dose estimate D_{E1} of 28.01 ± 0.84. The D_{max}/D_{E1} ratio (70.0) is, however,

significantly above the range of 5-10 recommended by Duval and Grün (2016) to avoid any dose overestimation. When using an adjusted D_{max} of 294 Gy (D_{max}/D_{E2} = 10.2), the D_E slightly increases by <1 Gy. Finally, SSE fitting with data weighting by $1/s^2$ provides a smaller, but consistent, D_{E3} by about 2 Gy. These results indicate that the different fitting options have a limited impact on the D_E results and show the robustness of the fitting results obtained for #11C. Consequently, the combined U-series/ESR age calculation is performed using D_{E2}.

S3.6.3 Dose rate considerations

S3.6.3.1 Evaluating the radioactivity of the sedimentary environment

The supposed locality of origin of the fossils is currently under water and no longer accessible (Figure 1). Consequently, the dose rate can only be tentatively reconstructed from the sediment taken from the specimens and from an accessible outcrop sediment in the area. The various sediment samples collected from both fossils and the field show very distinct facies and colours (Table S1), supporting the suggestion they derive from different units in the Ranggam Group. Nevertheless, the orange-yellow colour of the sediment surrounding BANG19-10 (sed #10A; Figure S1) is visually similar to the sediment collected *in situ* (Figure 1), suggesting that the tooth may have been originally embedded in, or at least sitting on, the Ranggam Formation rather than embedded in the Residual Gravel, contra Ko Ko (1986).

Radioelement concentrations are highly variable among sediment samples (Table S1). In particular ICP-MS analyses return unexpectedly high Th concentrations (from 70 to 268 ppm) for the sediment samples attached to the teeth (sed #10B, sed #10C and sed #11). This results in high and highly variable gamma dose rates ranging from 3,140 to 11,163 μGy/a. At this stage, the reliability of these data may be reasonably questioned, as analyses were performed with a very limited amount of material (Table S1), i.e. well below the minimum standards usually accepted (200 mg). Additionally, it is unlikely that such a small quantity is fully representative of the whole sedimentary environment surrounding the tooth. In contrast, the sediment collected in the field yields much lower radioelement concentrations, resulting in a significantly smaller gamma dose rate (Table S1). Consequently, given the variability observed among samples, initial combined U-series/ESR calculation are carried out using average radioelement concentrations from the 4 samples analysed by ICP-MS.

S3.6.3.2 Gamma dose rate attenuation and self-irradiation

Our Geant4 gamma dose rate simulations performed return similar attenuation and self-irradiation factors for the enamel samples #11A and #11C (Table S4). In particular, the

contribution of the tooth itself to the gamma dose rate corresponds to 0.079 (#11A) and 0.088 (#11C) of the infinite matrix gamma dose rate value derived from corresponding ^{238}U-series in dentine (note that dental tissues are typically free of Th and K). This indicates that the tooth itself does provide a small, yet quantifiable, contribution to the gamma dose rate, which was expected given its size (Grün, 1992). In comparison, the contribution of the sediment to the gamma dose rate of samples #11A and #11C corresponds to 0.59-0.57, 0.57-0.55 and 0.60-0.55 of the infinite matrix gamma dose rate values derived from K, U-series and Th-series concentrations in the sediment. These values vary within narrow range for sample #11C (0.55-0.57), and an average gamma attenuation factor of 0.56 ± 0.07 (which accounts for a water content of 20 ± 10 % in the sediment) may therefore be reasonably considered in the first instance. This value is significantly higher than the attenuation factor of 0.42 initially estimated for an elephant tooth by Debuyst et al. (2000) assuming an attenuation of 1.2% /mm (Aitken et al., 1985) and without including water attenuation.

Given the above, the gamma dose rate contribution from the sediment may be estimated to 5151 ± 357 µGy/a when using average radioelement concentrations from the four sediment samples and considering infinite-matrix conditions. With the average gamma attenuation factor of 0.56 ± 0.07, this contribution may be corrected to 3558 ± 509 µGy/a. In contrast, the contribution from the tooth to the dose absorbed by enamel sample #11C may be estimated to between < 0.5 µGy/a and 21.4 ± 1.2 µGy/a when considering either 0.04 ppm (outer dentine #11C) or 2.31 ppm (inner dentine #11C) of uranium in the dentine. A maximum self-irradiation dose of 153 ± 8.7 µGy/a may be estimated when considering an extreme scenario with the 20.2 ppm of U in the inner dentine of #11A. Moreover, these various values should also be regarded as maximum possible estimates, since they are based on the assumption of equilibrium in the ^{238}U-series. Regardless, in all cases these values are negligible in comparison with the contribution from the sediment, since they represent at best about 4%. Consequently, when considering an intermediate scenario based on the inner dentine of #11C being representative of the whole tooth, a total gamma dose rate of 3580 ± 509 µGy/a may be obtained in the first instance for combined U-series/ESR age calculation.

Table S1. Radioelement concentrations measured in the sediment samples by solution ICP-MS analyses. Key: n.a. = not applicable; n.m. = not measured, as the result of an insufficient amount of material. Gamma dose rates were obtained from the radioelement concentrations and using the conversion factors from Guérin et al. (2011) and an assumed long-term water content of 20%. No gamma attenuation factor was considered.

Sample	Tooth	Basic description	Quantity analysed (mg)	U (ppm)	Th (ppm)	K (%)	Gamma dose rate (µGy/a)
Sed #10A	BAN19-10	Orange silts	<10	n.m.	n.m.	n.m.	n.a.
Sed #10B	BAN19-10	Green clays	13	4.86 ± 0.18	105.21 ± 4.40	0.426 ± 0.017	4610 ± 316
Sed #10C	BAN19-10	Black coarse-grained sand (seems to be on top of sed #10B)	37	4.56 ± 0.17	69.7 ± 2.92	0.130 ± 0.005	3140 ± 218
Sed #11	BAN19-11	Similar to #10C	55	7.84 ± 0.28	268.33 ± 11.22	0.169 ± 0.007	11163 ± 763
BAN19-1	n.a.	Coarse sandstone to conglomerate with numerous clay ferruginous lenses.	200	2.15 ± 0.10	38.08 ± 1.59	0.187 ± 0.007	1709 ± 128

Table S2. Solution U-series dating results. Ratios in parentheses are activity ratios calculated from the atomic ratios but normalised to measured values of secular-equilibrium HU-1 (Ludwig et al. 1992). Errors are given at the 2σ level. ^{230}Th ages were calculated using Isoplot EX 3.0 (Ludwig 2003) with decay constants λ238 = 1.551x10^{-10} yr^{-1} for ^{238}U, λ234 = 2.826x10^{-6} yr^{-1} for ^{234}U and λ230 = 9.158x10^{-6} yr^{-1} for ^{230}Th (Cheng et al. 2000). 2σ errors in the uncorrected ages were propagated directly from the uncertainties in (^{230}Th/^{238}U) and (^{234}U/^{238}U). The corrected ^{230}Th age was calculated using an assumed bulk earth or upper crust value equivalent to a detrital ^{230}Th/^{232}Th activity ratio of 0.83.

Sample ID	Tissue	U (ppm)	^{232}Th (ppb)	^{230}Th/ ^{232}Th	^{230}Th/^{238}U	^{234}U/ ^{238}U	uncorr. ^{230}Th Age (ka)	corr. ^{230}Th Age (ka)
11A	enamel	0.0530 ± 0.0003	0.798 ± 0.003	125.7 ± 1.6	0.6232 ± 0.0084	1.2408 ± 0.0054	74.0 ± 1.5	73.7 ± 1.5
11A	dentine (outer)	0.0430 ± 0.0001	9.243 ± 0.036	8.92 ± 0.23	0.63169 ± 0.02057	1.3668 ± 0.0033	65.5 ± 2.2	61.0 ± 2.8
11A	dentine (inner)	20.245 ± 0.014	309.498 ± 0.343	73.25 ± 0.13	0.36905 ± 0.00058	1.5177 ± 0.0017	29.89 ± 0.07	29.60 ± 0.14
11C	enamel	0.0595 ± 0.0003	0.831 ± 0.004	260.8 ± 3.2	1.2004 ± 0.0144	1.2013 ± 0.0037	321 ± 21	321 ± 21
11C	dentine (outer)	0.0352 ± 0.0002	9.645 ± 0.048	8.44 ± 0.23	0.76308 ± 0.02057	1.7354 ± 0.0085	60.3 ± 2.1	55.9 ± 2.7
11C	dentine (inner)	2.3065 ± 0.0055	16.624 ± 0.024	171.70± 0.63	0.40788 ± 0.00168	1.2712 ± 0.0026	41.57 ± 0.23	41.41 ± 0.24

Table S3. ESR fitting results obtained for sample #11C. Intensity precision is expressed as the coefficient of variation associated to the mean ESR intensities derived from all the aliquots of a given sample after each repeated measurement. D_E precision is the variation (1 relative standard deviation) of the D_E values derived from the repeated measurements of a given sample. The minimum signal-to-noise (S/N) was estimated from the natural aliquot following the procedure described in Arnold et al. (2024).

Sample	**#11C**
Mean aliquot weight ± 1 s.d. (mg)	19.9 ± 0.3
Minimum S/N	7.4
Number of repeated measurements	2
Intensity precision (%)	0.1
D_E precision (%)	7.4
SSE fitting ($1/I^2$)	
D_{max} (Gy)	1960
Adj. r^2	0.999
D_{E1} (Gy)	28.01 ± 0.84 (3.0 %)
D_{max} / D_{E1}	70.0
SSE fitting ($1/I^2$)	
D_{max} (Gy)	294
Adj. r^2	0.999
D_{E2} (Gy)	28.87 ± 1.67 (5.8 %)
D_{max} / D_{E2}	10.2
SSE fitting ($1/s^2$)	
D_{max} (Gy)	294
Adj. r^2	0.999
D_{E3} (Gy)	26.95 ± 3.17 (11.8 %)
D_{max} / D_{E3}	10.9

Table S4. Gamma self-irradiation and attenuation factors induced by tooth BAN19-11 and calculated for samples #11A and #11C using Geant4 simulations. Each value corresponds to a fraction of the infinite-matrix gamma dose rate: the gamma self-irradiation factor is a fraction of the infinite-matrix gamma dose rate from the ^{238}U-series in the dentine (note that dental tissues are typically free of Th and K), while the gamma atenuation factors are a fraction of the infinite-matrix gamma dose rates from the ^{238}U-series, ^{232}Th-series and ^{40}K of the sediment. Values and associated errors include water attenuation based on a long-term water content of 5 ± 5 % and 20 ± 10 % (% dry weight) in the dentine and sediment, respectively, while secular equilibrium in the ^{238}U-series of the dental tissues and sediment has been assumed. Errors are 1σ.

Sample ID	Gamma self-irradiation (dose fraction for ^{238}U-series)	Attenuation factor (dose fraction for ^{40}K)	Attenuation factor (dose fraction for ^{238}U-series)	Attenuation factor (dose fraction for ^{232}Th-series)
#11A	0.079 ± 0.004	0.59 ± 0.07	0.57 ± 0.07	0.60 ± 0.07
#11C	0.088 ± 0.005	0.57 ± 0.07	0.55 ± 0.06	0.55 ± 0.07

Table S5. Data inputs and outputs for the combined U-series/ESR age calculation. All errors are given at a 1-σ confidence level. Post-Rn equilibrium was considered in dental tissues and sediment. Final D_E errors are made of a combination of errors from the fitting (Table 1) and the dose rate from the gamma source (2.3%).

SAMPLE	**#11C**
Enamel	
Dose (Gy)	28.9 ± 1.8
U (ppm)	0.060 ± 0.001
$^{234}U/^{238}U$	1.201 ± 0.002
$^{230}Th/^{234}U$	0.999 ± 0.055
Alpha Efficiency	0.13 ± 0.02
Water content (%)	0
Initial enamel thickness (µm)	2983 ± 298
Dentine (inner)	
U (ppm)	2.306 ± 0.002
$^{234}U/^{238}U$	1.271 ± 0.001
$^{230}Th/^{234}U$	0.321 ± 0.010
Water (%)	5 ± 3
Removed enamel thickness (µm)	85 ± 9
Dentine (outer)	
U (ppm)	0.035 ± 0.001
$^{234}U/^{238}U$	1.735 ± 0.004
$^{230}Th/^{234}U$	0.440 ± 0.036
Water (%)	5 ± 3
Removed enamel thickness (µm)	533 ± 53
Sediment	
U (ppm) [1]	4.85 ± 0.19
Th (ppm) [1]	120.3 ± 5.03
K (%)[1]	0.23 ± 0.01
Water (% dry weight)	20 ± 10
Depth (m)	5 ± 3
Combined U-series/ESR age calculations	
internal dose rate (µGy/a)	0
Beta dose rate, inner dentine (µGy/a)	0
beta dose rate, outer dentine (µGy/a)	0
Gamma dose rate (µGy/a)	3580 ± 509
Cosmic dose rate (µGy/a)	109 ± 32
Total dose rate (µGy a^{-1})	3689 ± 510
Age (ka)	7.8 ± 1.2

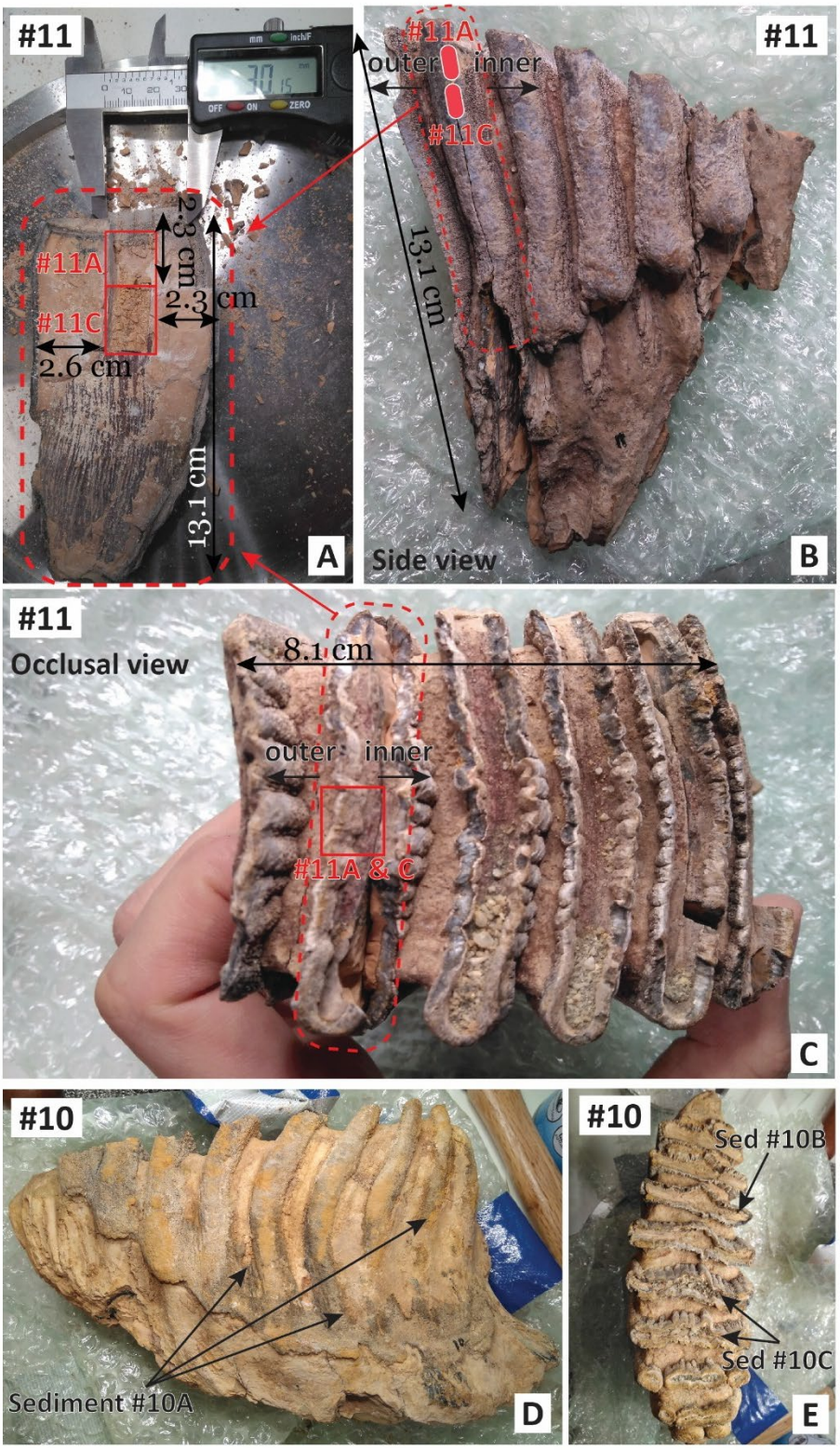

Figure S1. Sampling for ESR and U-series dating purpose. A to C: Tooth BAN19-11; D and E: BAN19-10 (pictures: M. Duval). The position of enamel samples #11A and #11C is indicated. U-series analyses were carried out on both #11A and #11C and the adjacent dentine layers, while only #11C was measured by ESR.

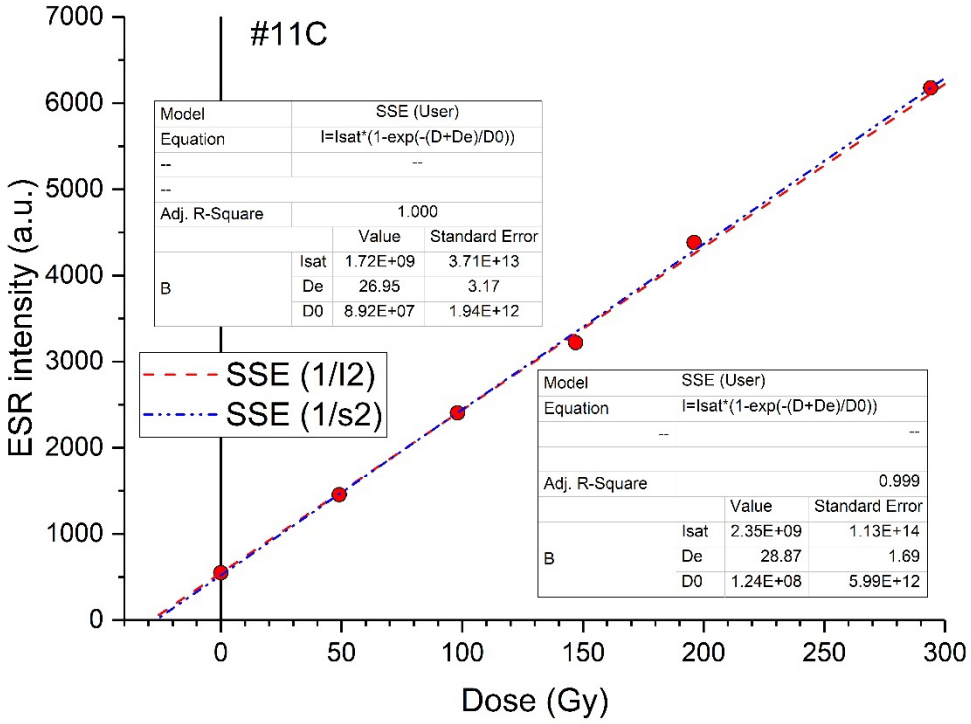

Figure S2. ESR dose response curve obtained for enamel sample #11C with D_{max} = 294 Gy used to meet the recommendations by Duval and Grün (2016).

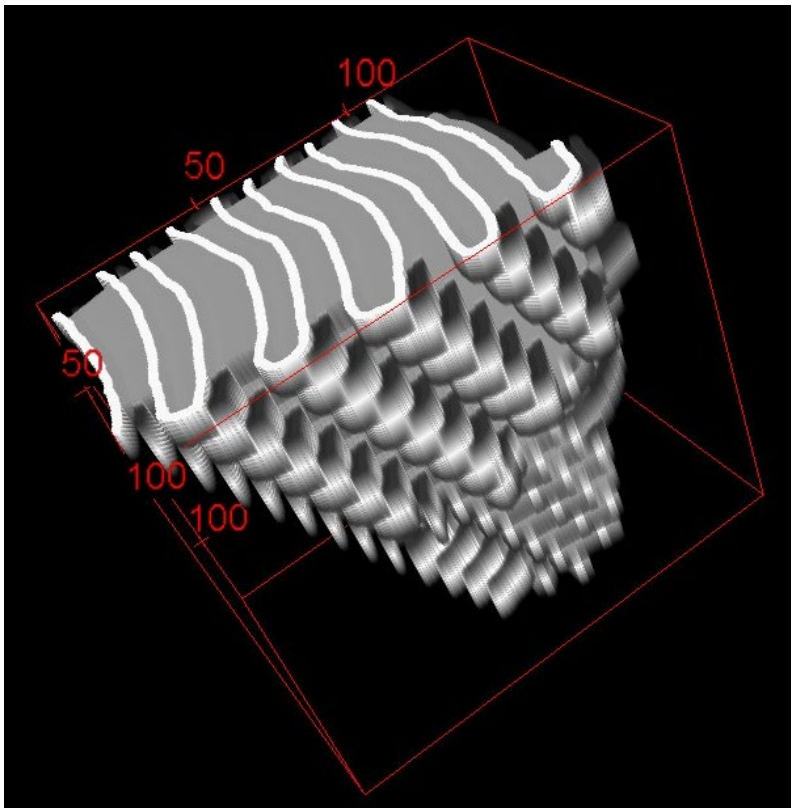

Figure S3. 3D model of tooth BAN19-11 used for the Geant4-based gamma dose rate simulations using DosiVox.

S4. Histology

A tooth fragment (Figure S5) measuring ca. 55 mm (length) x 33 mm (mesial-distal width) x 20 mm (occlusal width) was embedded in Buehler epoxy resin. A sectioning location for histology was marked on the resin block (Figure S6) which was cut along the lingual-buccal plane with a diamond blade on a Kemet 1500 low speed saw. A 'thick' section, measuring ~5 mm in thickness was extracted and glued onto a microscope glass slide using Stuck epoxy glue. Once dry, the section was trimmed on the low-speed saw to reduce it to a thickness of ~2 mm. The trimmed section was then ground down to ca. 100 μm using a series of grinding pads that had different levels of coarseness progressing from highly coarse to fine. The section was checked under a basic optical microscope for visibility and preservation of dental microstructure. Once the key histological characteristics were visible, the section was polished using a Buehler diamond powder paste, cleaned in an ultrasonic bath, dehydrated in a series of alcohol baths, and cleaned with xylene. A cover slip was then glued onto the slide.

The slide was imaged under a high-powered Olympus BX53 microscope equipped with a DP74 high resolution camera operated using the Olympus cellSens software. Long period Retzius lines and short period cross-striations, as well as the enamel-dentine junction (EDJ), were identified and examined for visibility so that they could be measured. As all these microscopic structures were preserved in the specimens, they were used in the analysis of enamel growth extension rate calculation following the method outlined in ref[22], in turn based on Shellis (1984). This method uses measurements of the angles between the EDJ and Retzius lines (D) and enamel rods (I), and the width of enamel cross-striations (d), to calculate enamel growth occurring from the occlusal towards the basal tooth region (enamel extension rate):

$$c = d[(\sin I / \tan D) - \cos I]$$

Using the open-source FIJI/ ImageJ software (Schindelin et al. 2015), the above measurements were taken from thin section images captured from the mid-enamel region bordering the EDJ (Figure 4). Three neighbouring images as regions of interest (ROIs) along the EDJ were taken and each image was examined independently by two histologists (PB, JJM) to account for possible inter-observer measurement errors. In addition, PB repeated her measurements twice to also account for any possible intra-observer error. Any disagreeing measurements were removed from the study, otherwise the repeat measurements from different observers were combined and averaged. Cross-striation width (d) was measured

directly in each image (Figure S7a) using the 'straight line' tool in FIJI/ImageJ from eight individual cross-striation distances. In two ROI images, one observer (PB) identified nine consecutive clear cross-striations instead of eight, so all nine were measured. Each eight measurements were repeated three times, and an overall average was calculated for each ROI. The three ROIs were then averaged so that one mean d value was obtained. The angles of D and I (Figure S7b-c) were measured using the 'angle' tool in FIJI/ImageJ. These were repeated three times in each ROI and an average calculated from all ROIs combined.

The final calculation of the enamel extension rate was obtained from a total of nine iterations (three observer measurements with three ROIs each). The resulting values were compared to values reported in previous publications dealing with *Mammuthus columbi*, *E. maximums*, and *Palaeoloxodon cypriotes* (Extended Table 3).

The raw data for individual measurements (d, I, D) in each ROI and from each observer are shown in Table S7, and the averages from these data for each observer, and combined, are shown Table S8.

Table S7. Raw data for individual measurements and from each observer: d – width of enamel cross-striations, D – the angle between EDJ and Retzius lines, I – the angle between EDJ and enamel rods (I).

Region of interest (image) 1									
Observer	**Observer 1**			**Observer 2a**			**Observer 2b**		
Repeat	First	Repeat 1	Repeat 2	First	Repeat 1	Repeat 2	First	Repeat 1	Repeat 2
Variable d (μm)	4.922	3.413	2.636	2.814	3.809	3.668	2.828	3.01	3.632
	2.763	2.677	2.702	4.699	3.1	1.931	2.5	1.953	3.944
	3.131	2.956	2.487	2.693	2.039	4.04	2.85	3.052	3.026
	3.514	3.512	3.244	2.751	2.924	3.298	3.202	2.85	3.223
	1.676	3.364	2.453	2.751	2.481	3.09	2.828	3.536	3.748
	2.401	2.464	3.63	3.278	1.95	3.955	2.828	2.01	3.48
	3.028	2.903	3.113	2.693	2.063	2.436	2.475	3.052	2.716
	2.801	2.558	3.127	2.309	2.063	4.04	2.658	3.26	3.741
D (degree)	5.556	5.871	8.13	6.618	6.521	6.202	5.484	6.255	5.544
I (degree)	46.67	56.655	45.974	43.238	39.417	43.736	43.457	40.649	37.37
Region of interest (image) 2									
d (μm)	2.245	1.642	2.113	1.907	2.323	3.687	3.283	3.162	2.749
	2.379	2.257	2.413	3.001	1.69	2.764	3.902	3.48	2.028
	2.314	1.898	2.307	2.47	1.768	3.481	3.283	1.944	2.848
	2.109	1.86	2.585	3.38	2.948	2.432	3.283	3.018	3.162

	2.147	2.294	2.461	2.221	2.323	2.284	3.073	3.073	1.795
	1.709	1.932	2.223	1.958	2.563	3.388	3.283	3.073	2.427
	2.271	2.155	2.039	2.221	2.906	3.063	3.48	2.749	1.795
	2.487	2.116	2.34	3.221	2.221	3.042	2.981	2.357	2.236
							2.848	2.539	3.727
D (degree)	5.691	5.995	7.903	6.951	6.178	6.09	6.119	6.782	7.688
I (degree)	46.654	46.026	55.827	46.862	48.171	50.893	51.739	43.213	48.835
Region of interest (image) 3									
D (µm)	2.591	3.106	3.512	2.044	4.425	3.159	2.863	2.426	2.239
	2.767	2.828	2.694	2.493	2.617	3.385	3.059	3.359	2.93
	2.878	3.642	2.72	2.482	3.951	4.176	3.345	4.224	3.541
	2.587	2.581	2.907	2.968	3.415	2.493	3.472	3.635	2.635
	2.209	2.742	2.718	1.471	2.942	3.167	3.106	3.514	3.891
	2.021	2.245	3.484	2.493	2.523	3.611	3.727	3.197	2.672
	2.581	2.894	2.812	2.482	2.708	3.049	3.106	3.345	3.541
	2.636	2.039	3.138	2.372	2.841	3.725	3.416	3.514	3.74
							3.727	2.653	4.479
D (degree)	5.574	5.827	6.063	5.952	6.07	5.962	6.712	6.448	6.45
I (degree)	46.63	45.448	53.687	49.942	42.925	41.641	39.376	41.548	45.307

Table S8. Summary of averaged measurements of d – width of enamel cross-striations, D – the angle between EDJ and Retzius lines, I – the angle between EDJ and enamel rods (I), with calculated enamel extension rates (c) and an enamel extension rate estimate in mm per year.

	ROI image	**d (µm)**	**D (degree)**	**I (degree)**	**c (µm/day)**	**Enamel extension-rate estimate (mm/yr)**
Observer 1	1	2.978	6.519	49.766	18.008	6.573
	2	2.179	6.530	49.502	13.113	4.786
	3	2.764	5.821	48.588	18.497	6.751
Observer 2a	1	2.953	6.447	42.130	15.344	5.601
	2	2.636	6.406	48.642	15.926	5.813
	3	2.958	5.995	44.836	17.763	6.483
Observer 2b	1	3.017	5.761	40.492	17.094	6.239
	2	2.873	6.863	47.929	15.839	5.781
	3	3.309	6.537	42.077	16.823	6.14
Average		2.852	6.320	45.996	16.490	6.019

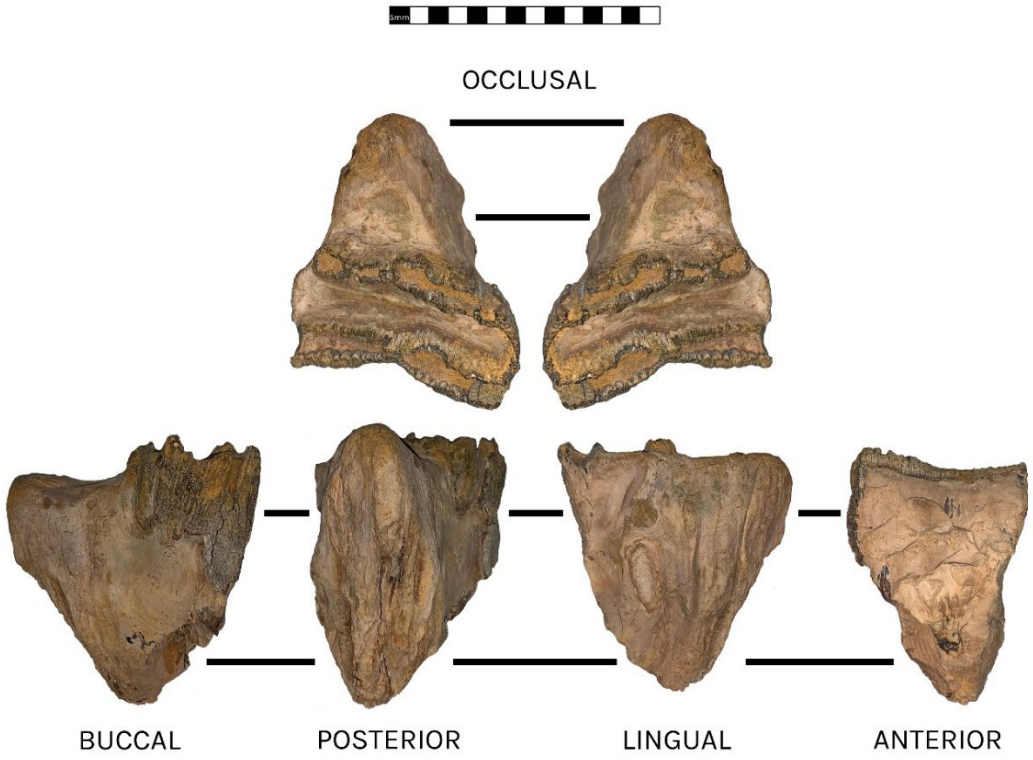

Figure S4. BAN19-12 elephant molar fragment examined for histology (scale bar 5 mm).

Figure S5. The tooth fragment from BAN19-12 selected for histology (scale bar 5 mm).

Figure S6. Tooth fragment selected for histological preparation. The red line indicates sectioning location.

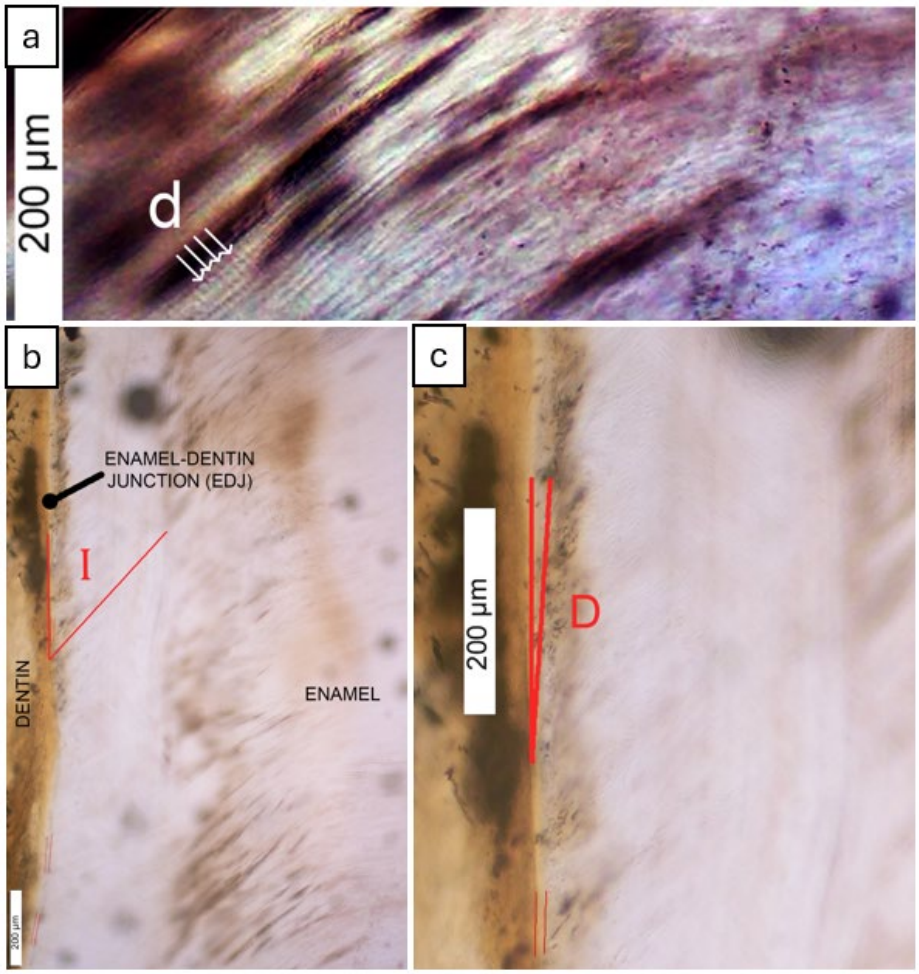

Figure S7. Regional enamel histology showing the components of enamel extension rate calculation: a) cross-striation width (d) with white arrows pointing to individual prisms, b) angle (I) between the enamel-dentine junction (EDJ) and enamel rods extending towards the outer enamel surface, and c) angle (D) between EDJ and the first/nearest Retzius line.

S5. Supplementary References

Aitken, M.J. (1985). Thermoluminescence Dating. London, Academic Press.

Arnold, L.J., Demuro, M., Duval, M., Grün, R., Daura, J., Sanz, M., Costa, A.M., Araújo, A.C. (2024). Single-grain luminescence and U-series/ESR dating of the early Upper Palaeolithic Lagar Velho Rock Shelter. Quaternary Geochronology 83: 101572. https://doi.org/10.1016/j.quageo.2024.101572.

Bahain, J.-J., Yokoyama, Y., Falguères, C. and Sarcia, M.N. (1992). ESR dating of tooth enamel: A comparison with K-Ar dating. Quaternary Science Reviews 11(1): 245-250.

Cheng, H., Edwards, R.L., Hoff, J., Gallup, C.D., Richards D.A., and Asmerom, Y. (2000). The half-lives of uranium-234 and thorium-230. Chemical Geology 169:17–33. doi.org/10.1016/s0009-2541(99)00157-6

Clark, T. R., Roff, G., Zhao, J. X., Feng, Y. X., Done, T. J., & Pandolfi, J. M. (2014). Testing the precision and accuracy of the U–Th chronometer for dating coral mortality events in the last 100 years. Quaternary Geochronology, 23: 35-45.

Debuyst, R., Callens, F., Frechen, M. and Dejehet, F. (2000). ESR Study of elephant tooth enamel from the Kärlich-Seeufer site in Germany. Applied Radiation and Isotopes 52(5): 1327-1336.

Duval, M. and Grün, R. (2016). Are published ESR dose assessments on fossil tooth enamel reliable? Quaternary Geochronology 31: 19-27.

Duval M., Fang F., Suraprasit K., Jaeger J.-J., Benammi M., Chaimanee Y., Iglesias Cibanal J., Grün R. (2019). Direct ESR dating of the late Middle Pleistocene vertebrate assemblage from Khok Sung locality, Nakhon Ratchasima Province, Northeast Thailand. Palaeontologia Electronica 22: 1-25. https://doi.org/10.26879/941

Grün, R. (1992). Suggestions for minimum requirements for reporting ESR age estimates. Ancient TL 10(3): 37-41.

Grün, R. (2000a). Methods of dose determination using ESR spectra of tooth enamel. Radiation Measurements 32: 767-772.

Grün, R. (2000b). An alternative model for open system U-series/ESR age calculations: (closed system U-series)-ESR, CSUS-ESR. Ancient TL 18: 1-4.

Grün, R. and Invernati, C. (1985). Uranium accumulation in teeth and its effect on ESR dating—A detailed study of a mammoth tooth. Nuclear Tracks and Radiation Measurements (1982) 10: 869-877.

Grün, R. and Brumby, S. (1994). The assessment of errors in past radiation doses extrapolated from ESR/TL dose-response data. Radiation Measurements 23: 307-315.

Grün, R. and Katzenberger-Apel, O. (1994). An alpha irradiator for ESR dating Ancient TL 12(2): 35-38 (1994).

Grün, R., Schwarcz, H.P. and Chadam, J. (1988). ESR dating of tooth enamel: Coupled correction for U-uptake and U-series disequilibrium. International Journal of Radiation Applications and Instrumentation. Part D. Nuclear Tracks and Radiation Measurements 14(1–2): 237-241.

Ludwig, K.R. (2003). *User's Manual for Isoplot/Ex Version 3.0: A Geochronological Toolkit for Microsoft Excel*. Berkeley Geochronology Centre, Berkeley.

Ludwig, K.R., Simmons, K.R., Szabo, B.J., Winograd, I.J., Landwehr, J.M., Riggs A.C., Hoffman R.J. (1992). Mass-spectrometric ^{230}Th-^{234}U-^{238}U dating of the Devils Hole calcite vein. Science 258:284–287. doi.org/10.1126/science.258.5080.284

Marsh, R.E. (1999). Beta-gradient Isochrons Using Electron Paramagnetic Resonance: Towards a New Dating Method in Archaeology. MSc thesis, McMaster University.

Martin, L., Mercier, N. and Incerti, S. (2015). DosiVox: a Geant 4-based software for dosimetry simulations relevant to luminescence and ESR dating techniques. Ancient TL 33(1): 1-10.

Price, G.J., Feng, Y.X., Zhao, J.X. and Webb, G.E., 2013. Direct U–Th dating of vertebrate fossils with minimum sampling destruction and application to museum specimens. Quaternary Geochronology 18: 1-8.

Shao, Q., Bahain, J.-J., Falguères, C., Dolo, J.-M. and Garcia, T. (2012). A new U-uptake model for combined ESR/U-series dating of tooth enamel. Quaternary Geochronology 10: 406-411.

Shao, Q., Bahain, J.J., Dolo, J.M. and Falguères, C., 2014. Monte Carlo approach to calculate US-ESR age and age uncertainty for tooth enamel. Quaternary Geochronology 22: 99-106.

Shellis, R. P. (1984). Variations in growth of the enamel crown in human teeth and a possible relationship between growth and enamel structure. Archives of Oral Biology 29: 697-705.

Zhao, J. X., Yu K. F., Feng Y. X., 2009. High-precision ^{238}U-^{234}U-^{230}Th disequilibrium dating of the recent past: A review. Quaternary Geochronology 4: 423-433.